

# SMPD: A soil moisture-based precipitation downscaling method for high-resolution daily satellite precipitation estimation

Kunlong He<sup>1,2</sup>, Wei Zhao<sup>1,\*</sup>, Luca Brocca<sup>3</sup>, Pere Quintana-Seguí<sup>4</sup>

<sup>1</sup>Institute of Mountain Hazards and Environment, Chinese Academy of Sciences, Chengdu 610041, China

<sup>2</sup>School of Civil Engineering, Sun Yat-sen University, Guangzhou 510275, China;

<sup>3</sup>Research Institute for Geo-Hydrological Protection, National Research Council, Perugia, Italy

<sup>4</sup>Ebro Observatory (OE), Ramon Llull University – CSIC, Roquetes, Spain.

**Correspondence:** Wei Zhao (zhaow@imde.ac.cn)

**Abstract.** As a key component in the water and energy cycle, precipitation with high resolution and accuracy is of great significance for hydrological, meteorological, and ecological studies. However, current satellite-based precipitation products have a coarse spatial resolution (from 10 to 50 km) not meeting the needs of several applications (e.g., flash floods and landslides). The implementation of spatial downscaling methods can be a suitable approach to overcome this shortcoming. In this study, we developed a Soil Moisture-based Precipitation Downscaling (SMPD) method for spatially downscaling the Integrated Multi-satellite Retrievals for GPM (IMERG) V06B daily precipitation product over a complex topographic and climatic area in southwestern Europe (Iberia Peninsula), in the period 2016-2018. By exploiting the soil water balance equation, high-resolution surface soil moisture (SSM) and Normalized Difference Vegetation Index (NDVI) products were used as auxiliary variables. The spatial resolution of the IMERG daily precipitation product was downscaled from 10 km to 1 km. An evaluation using 1027 rain gauge stations highlighted the good performance of the downscaled 1 km IMERG product compared to the original 10 km product, with a correlation coefficient of 0.61, root mean square error (RMSE) of 4.83 mm and a relative bias of 5%. Meanwhile, the 1 km downscaled results can also capture the typical temporal and spatial variation behaviors of precipitation in the study area during dry and wet seasons. Overall, the SMPD method greatly improves the spatial details of the original 10 km IMERG product with also a slight enhancement of accuracy. It shows good potential to be applied for the development of high-quality and high-resolution precipitation products in any region of interest.

**Keywords:** GPM; SMPD; surface soil moisture; spatial downscaling; daily precipitation

## 1 Introduction

Precipitation, as a key driving force of the global water cycle under climate change conditions, changes greatly in space and time and is among the key factors affecting the hydrology, water resources and ecosystem of a watershed (Salzmann, 2016; Spötl et al., 2021). Hence, accurate and reliable spatial-temporal precipitation estimates are critical for

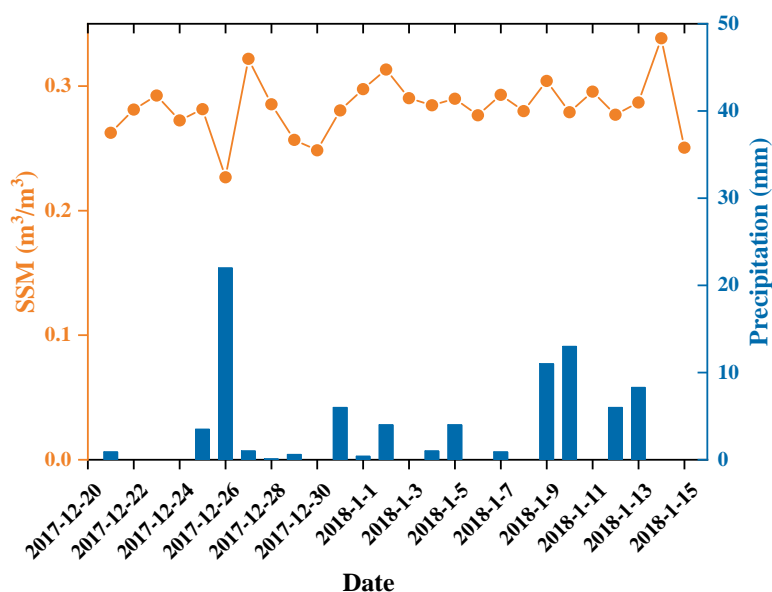
31 the assessment and understanding of climate change, hydrology, climatology, and its impacts on the environment,  
32 ecosystem, and human society (Xia et al., 2015; Wehbe et al., 2020; Wei et al., 2020; Bezak et al., 2021; Ma et al., 2021;  
33 Yang and Huang, 2021).

34 The most common ground-based method for precipitation measurement relies on rain gauge observations. Although  
35 rain gauges can provide accurate observations and capture the temporal variability in precipitation within a certain radius,  
36 these measurements are known to be prone to spatial representativeness issues due to the high spatiotemporal  
37 heterogeneity of precipitation (Wehbe et al., 2017; Tang et al., 2018). With the development of meteorological satellites,  
38 remote sensing has become the main tool for estimating regional to global precipitation because of its wide spatial  
39 coverage and continuous observation periods. These series of satellites include the Global Precipitation Climatology  
40 Project (GPCP) (Huffman et al., 1997), the Tropical Rainfall Measuring Mission (TRMM) Multisatellite Precipitation  
41 Analysis (TMPA) (Huffman et al., 2007), the NOAA Climate Prediction Center (CPC) morphing technique (CMORPH)  
42 (Joyce et al., 2004), Precipitation Estimation from Remotely Sensed Information using Artificial Neural Networks  
43 (PERSIANN) (Sorooshian et al., 2000), Global Satellite Mapping of Precipitation (GSMaP) (Kubota et al., 2007), and  
44 Integrated Multisatellite Retrievals for Global Precipitation Measurement (GPM) (Hou et al., 2014). Although each  
45 product has its strengths in the capture of precipitation spatial patterns, there is a common issue, induced by its coarse  
46 spatial resolution (e.g.,  $0.1^{\circ}$ - $0.5^{\circ}$ ), greatly blocking the application of these products in hydrological and meteorological  
47 research at the local scale (Lin and Wang, 2011; Prakash et al., 2016; Chen et al., 2018).

48 To enhance the applications of current coarse-resolution precipitation products, a procedure that involves spatially  
49 downscaling these products to fine scales has become an important solution. In recent decades, many downscaling  
50 methods have been proposed with the use of different satellite precipitation products. There are two major categories of  
51 downscaling methods: statistical downscaling and dynamical downscaling (Maraun et al., 2010; Tang et al., 2016).  
52 Statistical downscaling methods are mainly conducted by building the explanatory ability of the precipitation spatial  
53 distribution with fine-scale predictors, including topographic, geographic, atmospheric and vegetation variables, with  
54 the use of traditional regression methods (Xu et al., 2015; Ma et al., 2019b; Mei et al., 2020), optimal interpolation  
55 techniques (Shen et al., 2014; Chao et al., 2018), multidata fusion (Rozante et al., 2020; Ma et al., 2021), spatial data  
56 mining algorithm (called cubist) (Ma et al., 2017b; Ma et al., 2017a), geographical ratio analysis (Duan and Bastiaanssen,  
57 2013; Ma et al., 2019a) and machine learning algorithms (He et al., 2016; Baez-Villanueva et al., 2020; Min et al., 2020).  
58 Due to their convenience and efficiency, these approaches are dominant in precipitation spatial downscaling research  
59 (Abdollahipour et al., 2021). Comparatively, dynamical downscaling refers to the use of regional climate models driven  
60 by global climate model output or reanalysis data to generate regional precipitation information (Rockel, 2015), which  
61 requires more information on internal mechanisms related to complex physical processes of precipitation, such as

62 atmospheric, oceanic and surface information (Tang et al., 2016). Hence, spatial downscaling is achieved by modelling  
63 the conditional distribution of precipitation at a fine scale to characterize the spatial structure of precipitation (Haylock  
64 et al., 2006; Munsi et al., 2021).

65 Among the existing methods, due to the computational efficiency and the consideration of orography and vegetation  
66 in precipitation distribution, the statistical downscaling methods have been widely used in recent years. Most of them  
67 were conducted with the use of predictors, such as topographic and vegetation factors (Immerzeel et al., 2009; Jia et al.,  
68 2011; Jing et al., 2016a; Zeng et al., 2021). However, these predictors do not have physical connections with precipitation,  
69 they act as important environmental variables influencing precipitation distribution. Consequently, the lack of the  
70 physical background of this type method may introduce high uncertainty to the downscaled results. Comparatively,  
71 surface soil moisture (SSM) presents an obvious and strong physical connection with precipitation via their coupling  
72 and feedback processes (Seneviratne et al., 2010). As indicated by Brocca et al. (2014). Precipitation is the main driver  
73 of SSM temporal variability. A sudden increase may occur in SSM after a rainfall pulse over a period of time, followed  
74 by a smooth recession limb driven by evapotranspiration and drainage. This relationship can be well reflected by an  
75 example of the time series of precipitation and SSM from Dec 26 to 28, 2017 at station BRAGANCA, Portugal (Figure  
76 1). A rapid increase in SSM occurs after these rainfall events. Then, the moisture condition gradually becomes drier  
77 when there is no further rainfall.



78  
79 **Figure 1. Time series of observed precipitation and satellite observed SSM at station BRAGANCA, Portugal.**

80 According to this feature, SSM shows a big advantage in estimating precipitation, and this connection was approved  
81 by the SM2RAIN method proposed by Brocca et al. (2013). Fan et al. (2021) also demonstrated the good performance  
82 of the SM2RAIN products over the Tibet Plateau (TP) where the terrain is complex and the surface cover is  
83 heterogeneous. Additionally, the Soil Moisture Analysis Rainfall Tool (SMART) proposed by Chen et al. (2012) also

84 improved the sub-monthly scale accuracy of a multidecadal global daily rainfall product with a lower root mean square  
85 error (-13%) and a higher probability of detection (+5%). Recent applications of this bottom-up approach further  
86 demonstrate the success of using SSM in precipitation estimation at coarse-resolution scales (Brocca et al., 2016;  
87 Ciabatta et al., 2017; Ciabatta et al., 2018; Brocca et al., 2019; Wehbe et al., 2020). Although there is a lagging effect of  
88 the changes in soil moisture to precipitation, the rainfall-runoff experiment conducted by Song et al. (2020) further  
89 confirmed this effect becomes small with the increase of the temporal aggregation interval and its impact is relatively  
90 small at daily time scale (Brocca et al., 2016). Thus, it should be a very promising solution to improve the accuracy of  
91 daily precipitation downscaling by introducing daily SSM in current downscaling schemes. However, the availability of  
92 high-resolution SSM data is very limited and most of the current SSM products have a spatial resolution of more than  
93 10 km (Peng et al., 2021), placing significant restrictions on these applications. Furthermore, suffering from an indirect  
94 physical connection between topographic and vegetation factors and precipitation at a coarse temporal scale. Thus, a  
95 large amount of downscaling research has been conducted at monthly or annual scales (Abdollahipour et al., 2021). In  
96 addition, although daily high-resolution precipitation data have been produced by different methods (Brocca et al., 2019;  
97 Hong et al., 2021), the use of high-resolution SSM data to improve the spatial resolution of satellite precipitation products  
98 for generating daily-scale high-resolution precipitation data based on physical mechanisms is less studied.

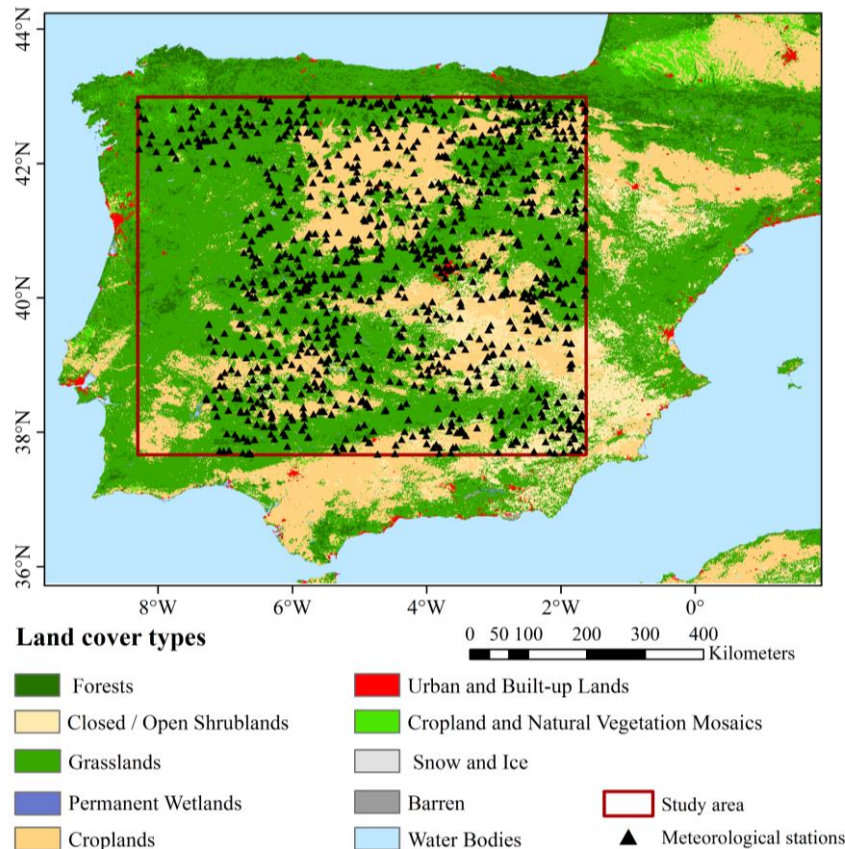
99 In recent decades, there have been substantial progress in soil moisture downscaling studies (Merlin et al., 2008;  
100 Piles et al., 2014; Peng et al., 2016; Tagesson et al., 2018; Long et al., 2019; Sabaghy et al., 2020; Wen et al., 2020; Zhao  
101 et al., 2021), which makes the availability of high-resolution soil moisture data possible at a daily scale. Thus, the main  
102 objective of this study is to establish a soil moisture-based precipitation downscaling (SMPD) scheme as a novel way of  
103 obtaining fine-scale precipitation by fragmenting the coarse-pixel rainfall into fine-scale pixels. For this purpose, the 25-  
104 km European Space Agency (ESA) Climate Change Initiative (CCI) SSM product is used to derive 1-km SSM data  
105 based on the seamless downscaling method proposed by Zhao et al. (2021). Based on the inversion of the water balance  
106 equation, a simplified model for estimating precipitation is constructed with the use of the downscaled 1-km seamless  
107 soil moisture data and the vegetation index derived from the Moderate Resolution Imaging Spectroradiometer (MODIS)  
108 observation and then applied to daily GPM precipitation products to obtain the daily downscaled precipitation estimates.

## 109 **2 Study area and datasets**

### 110 **2.1 Study area**

111 The central part of the Iberian Peninsula was selected as the study area (Figure 2). It is located in southwestern  
112 Europe between 37.66°–42.99°N and 8.30° W–1.63° E. The region has a distinctly seasonal mild climate, with hot and  
113 dry summers inland, cooler summers along the coast, and cold and wet winters. Precipitation presents a double peak

114 pattern, typical from the Mediterranean, with increased precipitation in Autumn and Spring. The central part of the study  
 115 area has a temperate continental climate, while the southern part has a Mediterranean climate, with warm and humid  
 116 winters and hot and dry summers. Generally, the south is dry and warm, while the north is relatively wet and cool.  
 117 Enhanced by the complex topographic pattern and diverse land cover conditions, this region has a highly heterogeneous  
 118 spatial environment, which makes this region a satisfactory candidate for precipitation downscaling. In addition, there  
 119 are many meteorological stations with long-term precipitation measurements in this area, which is an important  
 120 prerequisite for this study.



121 **Figure 2. Geolocation and land cover map of the study area. The black triangles denote the meteorological stations collected in this**  
 122 **study.**  
 123

124 **2.2 Datasets**

125 **2.2.1 GPM IMERG satellite precipitation data**

126 As the successor of the successful Tropical Rainfall Measuring Mission (TRMM), the Global Precipitation  
 127 Measurement (GPM) not only expands the measurement range and temporal and spatial resolution of the TRMM, but  
 128 also estimates the instantaneous precipitation more accurately, especially light-intensity precipitation (i.e.,  $<0.5 \text{ mm h}^{-1}$ )  
 129 and falling snow (Hou et al., 2014; Huffman et al., 2015), GPM-IMERG (Integrated Multisatellite Retrievals for GPM)  
 130 is the level 3 multisatellite precipitation algorithm of the GPM, which combines precipitation information measured from  
 131 the microwave sensor and infrared sensors onboard GPM constellations and monthly gauge precipitation data, and

132 IMERG employs the 2014 version of the Goddard Profiling Algorithm (GPROF2014) to compute precipitation estimates  
133 from all passive microwave (PMW) sensors onboard GPM satellites, which is a significant improvement compared with  
134 TMPA (GPROF2010) (Huffman et al., 2015; Huffman et al., 2020). Hence, it has attracted much attention in the satellite  
135 remote sensing of precipitation.

136 Currently, the GPM product provides near-real-time products (early and late run) and postural-rime products (final  
137 run) from sub-hourly to monthly resolution at a  $0.1^{\circ} \times 0.1^{\circ}$  spatial scale. Owing to the infusion of multiple data, such as  
138 microwave, infrared, radar, and Global Precipitation Climatology Centre (GPCC) rain gauge data (Hou et al., 2014), the  
139 GPM-IMERG final run product provides more accurate estimates over the globe with a relatively long time series (June  
140 2000- present) with a minimum latency of 3.5 months. In this study, the GPM-IMERG final run daily precipitation  
141 product (downloaded from <https://pmm.nasa.gov/data-access/downloads/gpm>) was adopted as the downscaling object.  
142 A three-year period from 2016 to 2018 was selected to verify the performance of the downscaling method based on the  
143 availability of rain gauge data.

#### 144 **2.2.2 ESA CCI surface soil moisture data**

145 The Soil Moisture CCI project is a part of ESA's Program on the Global Monitoring of Essential Climate Variables  
146 (ECV), which was initiated in 2010 and has produced an updated SSM product annually since 1978 (Colliander et al.,  
147 2017). The ESA CCI SSM series contains three separate SSM datasets, which are derived from active and passive  
148 microwave remote missions as well as a combination of both, and the combined ESA CCI SSM product (version 04.7)  
149 provides a spatial resolution of  $0.25^{\circ}$  and a temporal resolution of one day on a global scale (<http://www.esa-soilmoisture-cci.org/>).

151 The combined ESA CCI SSM product provides the amount of water in the surface soil (approximately the top 5  
152 cm), which integrates observations derived from 11 microwave sensors including active sensors such as Advanced  
153 Scatterometer-A/B (ASCAT-A/B) and European Remote-sensing Satellite-1/2 (ERS-1/2), and passive sensors such as  
154 Special Sensor Microwave Imager (SSM/I), the Scanning Multichannel Microwave Radiometer (SMMR), the TRMM  
155 Microwave Imager (TMI), AMSR-E, WindSAT, AMSR2 and SMOS (Gruber et al., 2019). Previous evaluation studies  
156 have demonstrated that ESA CCI SM generally agrees well with the spatial and temporal patterns estimated by land  
157 surface models and in situ observations (Mcnally et al., 2016; Dorigo et al., 2017). Therefore, this combined product  
158 was used in this study for the study period of January 1, 2016, to December 31, 2018, to obtain fine-resolution soil  
159 moisture to assist in precipitation downscaling.

### 160 2.2.3 Normalized difference vegetation index (NDVI)

161 NDVI is an important indicator of vegetation activity (Neinavaz et al., 2020; Zhang et al., 2020a; Pan et al., 2021),  
162 especially for surface evapotranspiration (Joiner et al., 2018; Maselli et al., 2020). Therefore, it also presents a positive  
163 correlation with precipitation (Quiroz et al., 2011; Birtwistle et al., 2016). The intuitive correlation between rainfall and  
164 plant biomass represented by NDVI would enhance the downscaling study with high-resolution NDVI data. In this study,  
165 the NDVI data were obtained from the MODIS/Terra 16-day vegetation index product  
166 (<https://lpdaac.usgs.gov/products/mod13a2v006/>). It is a 16-day composite product obtained by choosing the best  
167 available pixel value from all the acquisitions over 16 days with the spatial resolution of 1 km.

### 168 2.2.4 Rain gauge data

169 Daily precipitation data collected from 1027 rain gauge stations from 2016 to 2018 with different land cover  
170 properties were used as the independent validation of the downscaled results in this study. These data were provided by  
171 the Spanish State Meteorological Agency (AEMET). The distribution of the selected stations is mapped in Figure 2.

## 172 3 Methodology

### 173 3.1 Soil moisture-based precipitation estimation model

174 The soil water balance equation for a layer depth  $Z$  can be described by the following expression:

$$175 Z \frac{ds(t)}{dt} = p(t) - g(t) - e(t) - r(t) \quad (1)$$

176 where  $s(t)$  [-] is the relative saturation of the soil or relative SSM,  $t$  is the time and  $p(t)$ ,  $r(t)$ ,  $e(t)$  and  $g(t)$  are the  
177 precipitation, runoff, evapotranspiration, and drainage rate, respectively. By rearranging Eq. (1), precipitation can be  
178 depicted as a function of SSM, runoff, evapotranspiration, and drainage rate. Based on this rule, Brocca et al. (2013)  
179 proposed a bottom-up approach (SM2RAIN) by doing “hydrology backward” to infer precipitation with the use of  
180 variations in SSM sensed by microwave satellite sensors. To perform this estimation, the model is simplified in different  
181 ways by neglecting different components in Eq. (1) (Brocca et al., 2014; Massari et al., 2014) and the comparison study  
182 indicated that the average contribution of surface runoff and evapotranspiration components amounts to less than 4% of  
183 the total rainfall, while the soil moisture variation (63%) and subsurface drainage (30%) terms provide a much greater  
184 contribution (Brocca et al., 2015). Although the contribution of evapotranspiration is relatively small, the dry  
185 Mediterranean climate in most of this region emphasizes its importance. Therefore, the precipitation estimation model  
186 was reorganized by only neglecting the runoff component:

$$187 p(t) = Z \frac{ds(t)}{dt} + g(t) + e(t) \quad (2)$$

188 In Eq. (2), the drainage rate is approximated by considering the relation in Famiglietti and Wood (1994) to include the  
 189 contribution of both deep percolation and subsurface runoff (interflow plus baseflow):

$$190 \quad g(t) = as(t)^b \quad (3)$$

191 where  $a$  and  $b$  are two parameters expressing the nonlinearity between drainage rate and soil saturation. Regarding the  
 192 evapotranspiration component, there are many methods have been developed to estimate ET in natural ecosystems (Mu  
 193 et al., 2009; Sheffield et al., 2009; Carpintero et al., 2020). For instance, the daily evapotranspiration can be derived as  
 194 a function of the vegetation index ( $VI$ ) and air temperature ( $T_a$ ) (Nagler et al., 2005a; Nagler et al., 2005b):

$$195 \quad e(t) = a(1 - e^{-bVI}) \left( m / (1 + e^{-(T_a - d)/p}) + f \right) \quad (4)$$

196 where the coefficients ( $a$ ,  $b$ ,  $m$ ,  $d$ ,  $p$ , and  $f$ ) were determined by conducting regression between ET and the independent  
 197 variables. Although there is a variable representing air temperature in Eq. (4) to specify the impact of air temperature  
 198 difference within a wide range, this variable can be assumed to be invariant when considering the pixels to a small extent.  
 199 Therefore, the term with the second brackets of Eq. 4 is simplified to the coefficient  $c$ , and Eq. (4) is further rewritten as  
 200 follows by introducing NDVI to present the  $VI$  variable:

$$201 \quad e(t) = c(1 - e^{-kNDVI}) \quad (5)$$

202 Based on the above approximation, the soil moisture-based precipitation estimation model was finally expressed  
 203 by the following equation:

$$204 \quad p(t) = Z \frac{ds(t)}{dt} + as(t)^b + c(1 - e^{-kNDVI}) \quad (6)$$

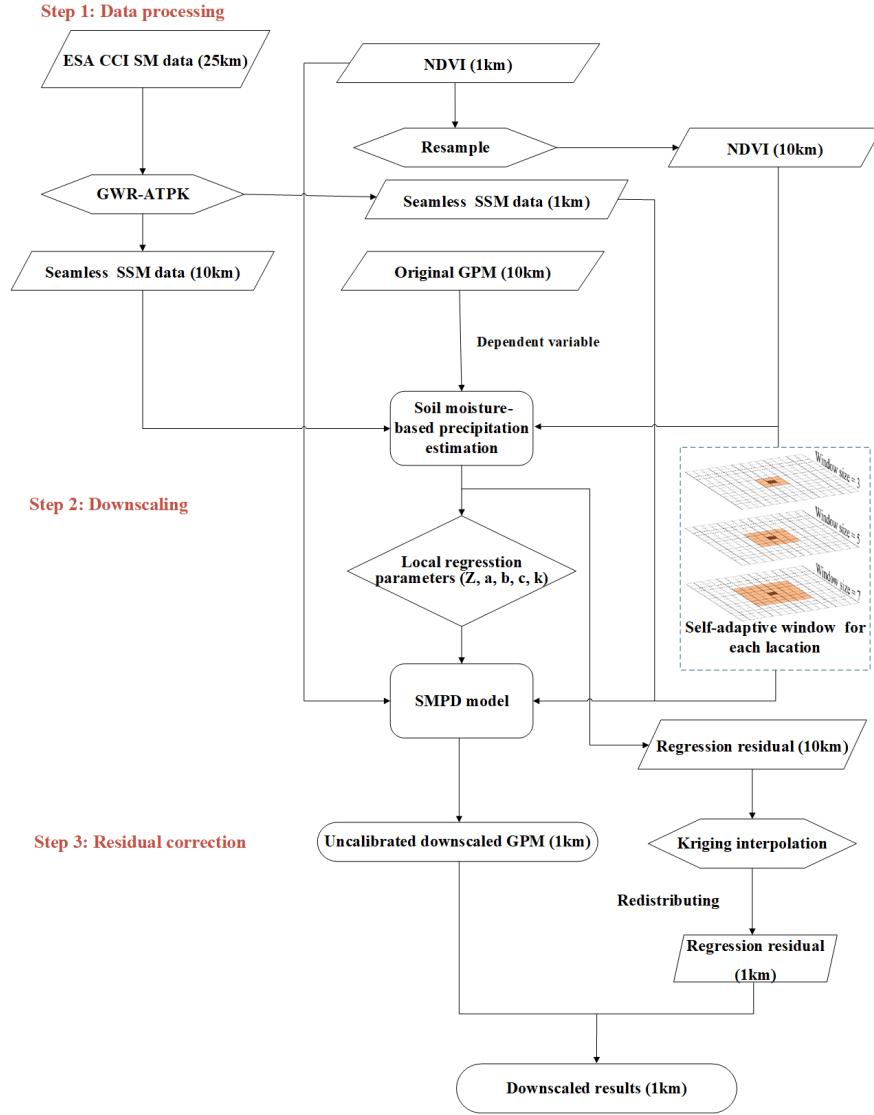
205 where  $ds(t)/dt$  can be calculated as the difference between the SSM estimates on nearby time steps. According to the  
 206 simplification in Eq. (6), this proposed model is appropriate for estimation to a local extent.

### 207 **3.2 Soil moisture-based precipitation downscaling (SMPD) method**

208 To perform precipitation downscaling, an important prerequisite is an assumption of spatial invariancy in the  
 209 precipitation estimation model described in Eq. (6) at coarse and fine scales, which is also the basis of many related  
 210 downscaling studies aiming at other surface parameters, such as soil moisture and temperature (Hutengs and Vohland,  
 211 2016; Mishra et al., 2018; Zhao et al., 2018; Ebrahimi and Azadbakht, 2019). Therefore, the estimation model  
 212 established at the 10-km level is thought to be applicable at the 1-km level. The estimated parameters  $Z$ ,  $a$ ,  $b$ ,  $c$  and  $k$  at  
 213 10 km resolution scale resolution are not scale-independent, which can be used for the corresponding sub-pixel units (1  
 214 km). Moreover, because the downscaled model was constructed by using self-adaptive windows in different local regions  
 215 on the daily scale, these parameters vary in time and space. Thus, they are also temporal independent. The fitted  
 216 estimation model at 10 km scale was applied to the SSM and NDVI data at 1 km scale to obtain the estimated high-



217 resolution precipitation. Then, to preserve the mean rain rate over each coarse-scale pixel, the bias was corrected by  
 218 redistributing the residual to each fine-scale pixel based on the kriging interpolation method. Finally, the downscaled  
 219 daily GPM precipitation products were obtained with the integration of the estimated precipitation and the interpolated  
 220 residual. According to the above principle, the downscaling method consists of the following parts and the main  
 221 procedures in the downscaling processes are shown in Figure 3.



222  
 223 Figure 3. Flowchart of the process for downscaling the GPM data from 2016 to 2018.

### 224 3.2.1 Generation of daily SSM at a fine resolution

225 As shown in Eq. (6), SSM is an important variable in the estimation model. The ESA CCI SSM product can only  
 226 provide coarse-resolution SSM data with unexpected gaps. To obtain daily SSM at a 1-km resolution, the seamless SSM  
 227 downscaling method proposed by Zhao et al. (2021) is a good choice to achieve this goal. In comparison to the  
 228 REMEDHUS network, the downscaled SSM performs better in terms of spatiotemporal coverage and evaluation metrics,  
 229 which indicated that this method could be successfully used to produce high-resolution SSM data with no spatiotemporal  
 230 gaps. This downscaling method mainly includes three steps: 1) filling gaps in the 25-km ESA CCI SSM maps with

231 neighbourhood information based on a local linear regression method, 2) estimating the 1-km regression SSM and  
 232 coarse-resolution residual with a geographically weighted regression (GWR) method, and 3) downscaling the coarse-  
 233 resolution residual to 1-km spatial resolution with the area-to-point kriging (ATPK) method and obtaining the fine-  
 234 resolution SSM. For details about the downscaling method, please refer to Zhao et al. (2021).

### 235 3.2.2 Calibration of the precipitation estimation model with an adaptive window method

236 Before model calibration, the 1-km downscaled SSM data and the NDVI data were first aggregated into a 10-km  
 237 scale to spatially match the spatial resolution of the GPM-IMERG product. Then, these data were applied to calibrate  
 238 the coefficients of the precipitation estimation model. As introduced in section 3.1, the application of this model requires  
 239 a prerequisite to work at a local extent because of the simplification of the evapotranspiration estimation. Therefore, a  
 240 local window with a radius from 3 to 7 cells was adopted in the fitting process. Initialized from the size of 3 cells, the  
 241 optimal window size was adaptively selected when the correlation coefficient (CC) of the fitting result reached the  
 242 maximum value. This adaptive method was applied to each coarse-resolution pixel with a sliding window, and the model  
 243 coefficients of this pixel were derived. During the model calibration, coarse pixels with zero precipitation were excluded.

$$244 \quad p_{10\text{km}}^m(t) = Z(SSM_{10\text{km}}(t) - SSM_{10\text{km}}(t-1)) + aSSM_{10\text{km}}(t)^b + c(1 - e^{-kNDVI_{10\text{km}}}) \quad (7)$$

### 245 3.2.3 Residual correction and fine-scale precipitation estimation

246 Based on the calibrated estimation model coefficients in Eq. 7, the precipitation estimates determined with this  
 247 model can be calculated for each high-resolution pixel within the corresponding coarse pixel:

$$248 \quad p_{1\text{km}}^m(t) = Z(SSM_{1\text{km}}(t) - SSM_{1\text{km}}(t-1)) + aSSM_{1\text{km}}(t)^b + c(1 - e^{-kNDVI_{1\text{km}}}) \quad (8)$$

249 However, there is a residual between the original precipitation value of each coarse-resolution cell pixel and the  
 250 mean value of the estimated precipitation of all fine-resolution pixels within this cell. For each coarse-resolution cell,  
 251 the residual is expressed as follows:

$$252 \quad R_{10\text{km}} = P_{10\text{km}}^o - P_{10\text{km}}^m \quad (9)$$

253 The kriging interpolation method was used here to interpolate residuals  $R_{10\text{km}}$  at coarse-resolution cells to obtain  
 254 kriging residuals fine-resolution scale (Wackernagel, 2003). The high-resolution residual was expressed as a weighted  
 255 integration of the residuals of the neighbouring coarse-resolution cells.

256 To meet the requirement of value preservation in the downscaling process, the kriging residuals should be corrected  
 257 by redistributing it to each fine-resolution pixel  $i$ . That is, the ratio of the  $i^{\text{th}}$  high-resolution residual pixel in the  $j^{\text{th}}$   
 258 coarse-resolution cell to the sum of the precipitation in the  $j^{\text{th}}$  coarse pixel is used as the weight  $\lambda_{ij}$ , and the residual  $R_{10\text{km}}$

259 is multiplied by the  $\lambda_{ij}$ , the kriging residuals were redistributed to each fine resolution pixel  $i$  to obtain the residual after  
 260 value preservation can be expressed as follows:

$$261 \quad R_{1\text{km},ij} = \lambda_{ij} R_{10\text{km},ij}, \text{ s. t. } \lambda_{ij} = \frac{P_{1\text{km},ij}^m}{\sum_{i=1}^n P_{1\text{km},ij}^m} \quad (10)$$

262 where  $R_{1\text{km},ij}$  represents the estimated precipitation of the  $i^{\text{th}}$  high-resolution residual pixel in the coarse-resolution cell  
 263  $j$ ,  $R_{10\text{km},ij}$  represents the  $j^{\text{th}}$  coarse-resolution cell residual in the self-adaptive window,  $n$  is the number of high-resolution  
 264 residual pixels in the coarse-resolution cell, and  $\lambda_{ij}$  is the weight coefficient of the  $i^{\text{th}}$  high-resolution residual pixel in the  
 265  $j^{\text{th}}$  coarse-resolution cell.  $P_{1\text{km},ij}^m$  is the kriging interpolated residual  $P_{1\text{km},ij}^m$  at the fine-scale pixel  $i$  in the  $j^{\text{th}}$  coarse-  
 266 resolution cell.

267 Finally, the high-resolution precipitation was obtained by integrating the fine-resolution estimates via Eq. (8) and  
 268 the residual term in Eq. (10):

$$269 \quad P_{1\text{km}} = P_{1\text{km}}^m + R_{1\text{km}} \quad (11)$$

### 270 3.3 Validation

271 To better assess the performance of the proposed downscaling method, the downscaled GPM results were validated  
 272 by observations from the collected stations in the study area at both daily and monthly scales. The evaluation metrics  
 273 include the correlation coefficient (CC), root mean square error (RMSE), and the relative bias (BIAS). They are defined  
 274 as follows:

$$275 \quad CC = \frac{\sum_{i=1}^n (S_i - \bar{S})(P_i - \bar{P})}{\sqrt{\sum_{i=1}^n (S_i - \bar{S})^2 (P_i - \bar{P})^2}} \quad (12)$$

$$276 \quad RMSE = \sqrt{\frac{\sum_{i=1}^n (S_i - P_i)^2}{n}} \quad (13)$$

$$277 \quad BIAS = \frac{\sum_{i=1}^n (S_i - P_i)}{\sum_{i=1}^n P_i} \quad (14)$$

278 where  $P_i$  and  $S_i$  are the precipitation measured by the rain gauge and satellite precipitation, respectively.  $i$  is the index of the  
 279 precipitation series.  $\bar{P}$  is the mean value of all rain gauge observations, and  $\bar{S}$  represents the mean value of the satellite  
 280 precipitation, and  $n$  represents the sample number of precipitation pairs.

281 Additionally, three metrics reflecting the capability of capturing precipitation events were introduced in the  
 282 assessment: the probability of detection (POD), the false alarm ratio (FAR) and critical success index (CSI). The POD  
 283 refers to the ratio of rain occurrences correctly detected to the total number of observed events; the optimum score is 1.  
 284 The FAR refers to the proportion of the precipitation events that the satellite falsely detects and the rain gauges do not  
 285 recognize it, the optimum score is 0. The CSI represents the fraction of precipitation events correctly detected by satellites  
 286 to the total number of observed or detected rainfall events, the optimum score is 1. The definition of a rainfall  
 287 accumulation “event” is one-day rainfall accumulation in excess of a given threshold of 0.1 mm. These three terms are  
 288 depicted as below:

$$289 \quad POD = \frac{H}{H + M} \quad (15)$$

$$290 \quad FAR = \frac{F}{H + F} \quad (16)$$

$$291 \quad CSI = \frac{H}{H + F + M} \quad (17)$$

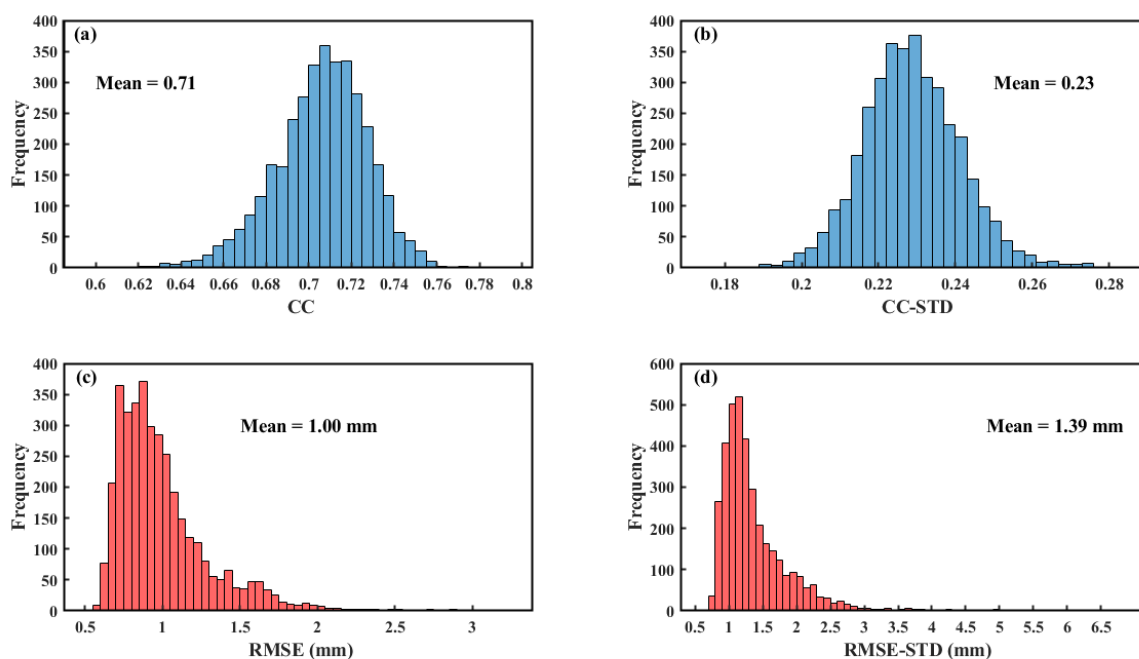
292 where  $H$  indicates the precipitation events concurrently detected by rain gauges and satellites,  $M$  indicates the  
 293 precipitation events detected by rain gauges but not detected by satellites, and  $F$  indicates the precipitation events  
 294 detected by satellites but not detected by rain gauges.

## 295 **4 Results**

### 296 **4.1 Accuracy of the soil moisture-based precipitation estimation model**

297 Before the downscaling process, the performance of the soil moisture-based precipitation estimation model was  
 298 evaluated first based on the calibrated estimation model in Eq. 7. Figure 4 shows the maps of the mean value of the daily  
 299 CCs and RMSEs during the period of 2016–2018 and their standard deviation (STD) by comparing the precipitation  
 300 estimated with the proposed estimation model and the GPM precipitation product at 10 km scale. Most of the CC values  
 301 are above 0.70 with an average value of 0.71, and most of the RMSE values are within the range from 0.50 to 1.00 mm,  
 302 with an average value of 1.00 mm. These results indicate the good consistency and small error between the estimated  
 303 precipitation and the original precipitation product. Furthermore, in view of the STD map, it represents the variability in  
 304 CC and RMSE during the period. The CC-STD values are within the range from 0.18 to 0.28 with an average value of  
 305 0.23, most of the RMSE-STD values are concentrated in the range of 0.50 to 1.50 mm, and only a few are in the range  
 306 of more than 3 mm, with an overall mean of 1.39 mm. Combined with the frequency distributions of CC and CC-STD,  
 307 RMSE, and RMSE-STD, the proposed estimation model can generally capture the precipitation with soil moisture  
 308 variations and it has relatively stable performance. According to the fitting performance assessment with the original

309 GPM product, the soil moisture-based precipitation estimation model has been approved to be able to capture the  
310 variation of precipitation with acceptable accuracy.

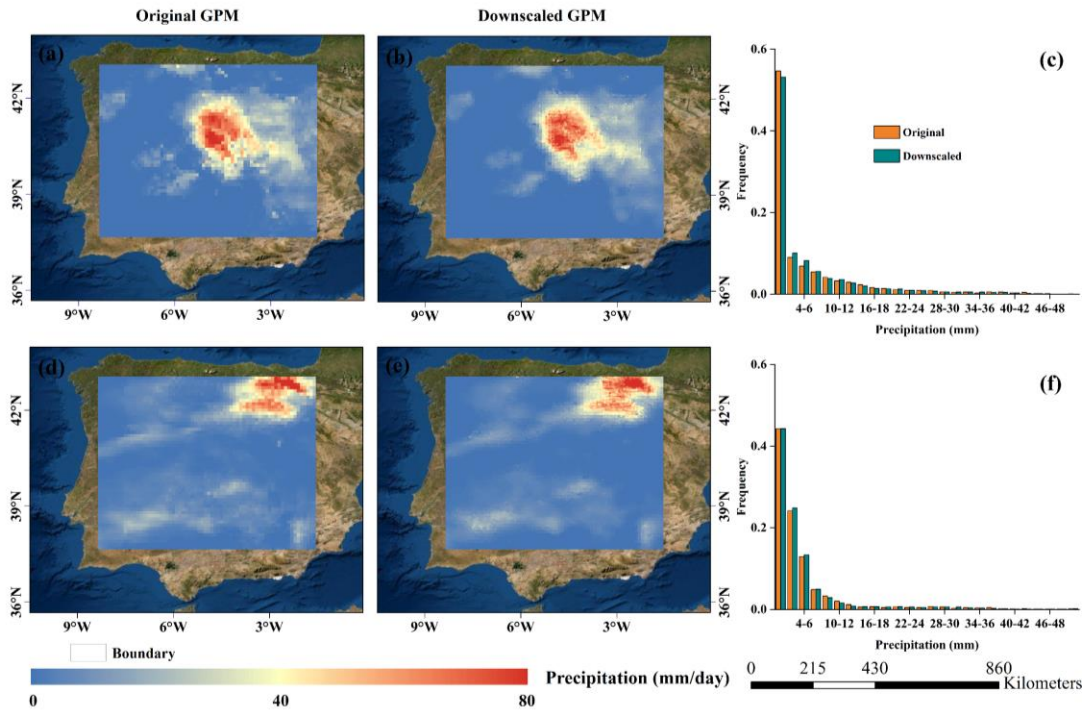


311  
312 **Figure 4. (a) Maps of the mean value of the correlation coefficient (CC), (b) mean standard deviation of the CC (CC-STD), (c) mean**  
313 **root mean square error (RMSE), and (d) mean standard deviation of the RMSE (RMSE-STD) between the precipitation estimated**  
314 **with the soil moisture-based estimation model and the original GPM product during the period of 2016-2018. The mean value**  
315 **represents the average value of the corresponding index in the whole study area.**

## 316 4.2 Overall performance of the downscaled precipitation

### 317 4.2.1 Spatial distribution

318 To demonstrate the advantages of the downscaling results, two separate days (Jul. 7 and Nov. 25, 2017) in the dry  
319 season and wet season were selected to compare the original coarse-resolution precipitation data and the downscaled  
320 high-resolution precipitation data (Figure 5). From the visual inspection, the spatial distributions of the downscaled  
321 precipitation are highly consistent with those of the original ones in both seasons, especially for the distribution of the  
322 precipitation centers (>50 mm/day). The downscaled results maintained the original precipitation pattern in the GPM  
323 product, which can be reflected well by the very similar histograms of the original and downscaled precipitation on these  
324 two days, as shown in Figures 4c and f. In addition to their consistency, the downscaled results present higher spatial  
325 heterogeneity than the coarse-resolution product, which provides much more detailed information on the precipitation  
326 distribution within each coarse-resolution cell. More importantly, the downscaled results prevent the blockiness at the  
327 edges of the coarse-scale pixels.

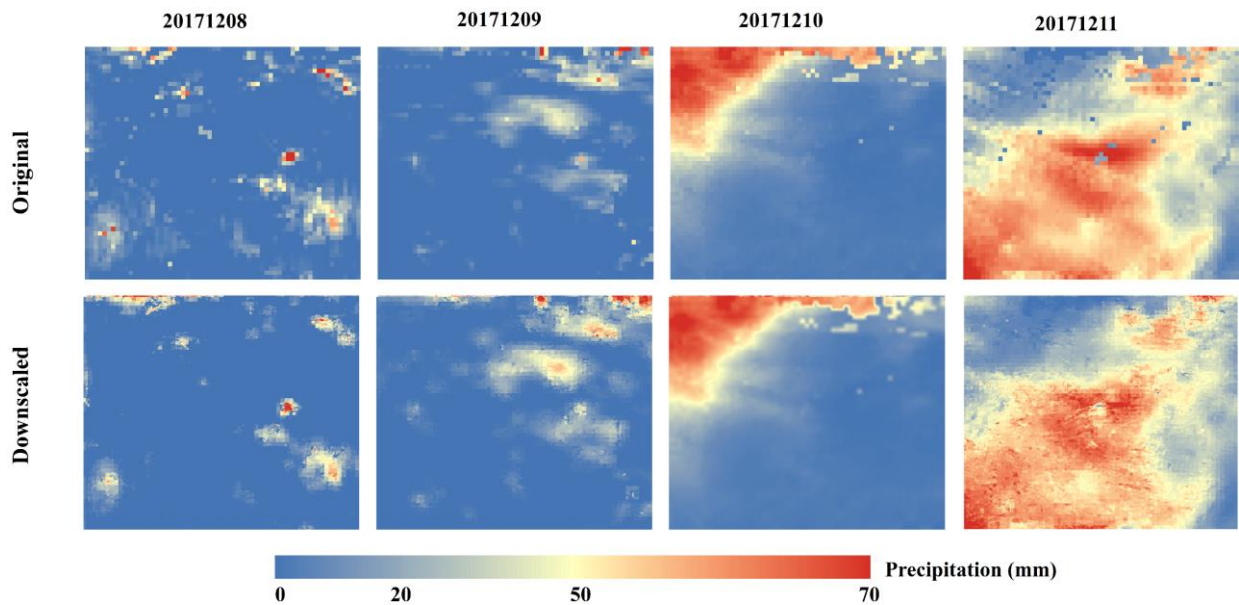


328

329 **Figure 5. Original daily GPM precipitation products, downscaled results, and their frequency histograms on July 7, 2017(a-c) and**  
 330 **November 25, 2017(d-f).**

331 **4.2.2 Temporal variability**

332 In addition to the spatial distribution analysis, the temporal variation in the downscaled precipitation was further  
 333 evaluated by introducing the downscaled results from Dec. 8 to Dec. 11, 2017. Figure 6 shows the daily maps of the  
 334 original precipitation and downscaled precipitation. For the spatial distribution, both the original GPM precipitation  
 335 product and the downscaled result have almost the same patterns on different days. Not only heavy rainfalls but also  
 336 light rainfalls and no rains can also be captured by the proposed downscaling method in most circumstances. Moreover,  
 337 the temporal variability in the daily precipitation was also preserved after the downscaling, and some outliers in the  
 338 coarse-resolution GPM product were effectively filled with valid values, as shown by the downscaling results on Dec.  
 339 11 in Figure 6.

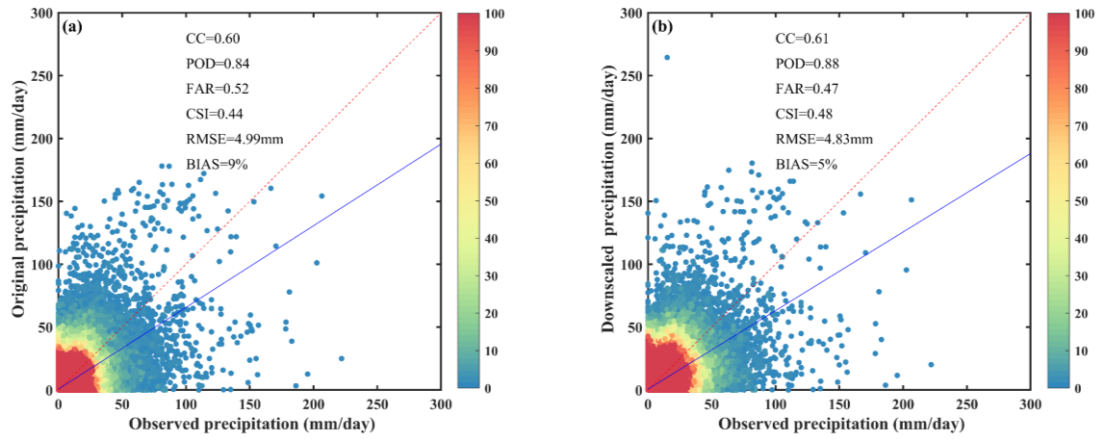


340  
341 **Figure 6. Original daily GPM precipitation product and corresponding downscaled results from Dec.8<sup>th</sup> to Dec.11<sup>th</sup>, 2017.**

342 **4.3 Validation with rain gauge measurements**

343 **4.3.1 Validation at the daily scale**

344 To quantitatively evaluate the performances of the downscaling results, the daily original-scale GPM precipitation  
 345 data and the downscaled results are compared separately with the precipitation measurements from all 1027  
 346 meteorological stations in the period of 2016 to 2018. Three metrics (POD, FAR, and CSI) for rainfall events, and CC,  
 347 RMSE and BIAS for precipitation volumes, were used to make a comparison between the performances of both datasets.  
 348 As shown by the density plots in Figure 7a, there is relatively high uncertainty in the original GPM precipitation product  
 349 compared with the in-situ observation with a CC of 0.60, an RMSE of 4.99 mm and a BIAS of 9 %, which shows the  
 350 GPM product generally overestimated observed precipitation at daily scale. These differences may be attributed to the  
 351 differences in the spatial representativeness of both observations (one for the average value over a grid cell and one for  
 352 a single point). Because of the value preservation during the downscaling process, the downscaled result also has a  
 353 validation effect similar to that of the original GPM precipitation product (Figure 7b). However, compared with the  
 354 original GPM product, the downscaled result shows an overall improvement in terms of CC, RMSE, and BIAS. There  
 355 is a slight increase in CC, with its value increasing from 0.60 to 0.61. In contrast, both the RMSE and BIAS have a  
 356 moderate reduction, with decreases of 0.16 mm and 4%, respectively. For rainfall event assessment, the downscaled  
 357 result remarkably enhanced the ability to identify rainfall events at every station when compared with the original GPM  
 358 product. Both the POD, FAR and CSI were moderately enhanced relative to those of the original GPM data, with an  
 359 increasing POD from 0.84 to 0.88, a decrease in the FAR from 0.52 to 0.47 and an increasing CSI from 0.44 to 0.48.  
 360 The comparison showed that the downscaled results could better detect precipitation occurrence than the original GPM  
 361 product. The increase in spatial heterogeneity in the downscaled result assists rainfall event detection.



362

363

364

365

**Figure 7. Scatterplots of the original GPM precipitation product (a) and the downscaled results (b) plotted against daily precipitation recorded by available meteorological stations over the study period. The red dotted line represents the 1:1 line and the blue solid line represents the fitting line.**

366

367

368

369

370

371

372

373

374

375

376

377

378

379

380

381

382

383

384

385

In addition to the validation during the period of 2016-2018, further investigation was performed for the downscaled results at individual months. Table 1 lists the evaluation indicators of the downscaled and original precipitation against rain gauge observations for 1027 in-situ measurements from 2016 to 2018. In general, the downscaled results show similar accuracy performance among different months from the detection accuracy of precipitation events reflected by FAR and CSI. It is worth noting that the POD decreased compared to the original precipitation product, which may be because compared with the coarse pixel precipitation at the daily scale, the downscaled products of the sub-pixels at the same in-situ measurements location do not necessarily have precipitation, resulting in fewer precipitation events detected by the downscaled products. From the RMSE values, seasonal differences can be detected. The dry season months from June to September have relatively smaller RMSE values than other months. It is not because of the better performance of the proposed method in these months but the inherent small precipitation of these months enables the low value of RMSE. This feature can be also detected from the evaluation of the original data. Regarding the downscaled results performance, the downscaled data have better accuracy in detecting precipitation events according to the improvement in FAR and CSI in each month. Comparatively, the correlation feature of the downscaled results shows a small improvement than the original data, represented by the CC values every month. Meanwhile, there are all decreasing trends in terms of RMSE and the improvements in the wet seasons from October to May are relatively bigger than in the dry season months. For the BIAS values, the improvements are also very clear with the extent from 3% to 7%. The monthly comparison further indicated the improvement from the downscaled results which not only maintain the temporal correlation characteristics of the original data with the gauge-based observations but also improve the absolute accuracy according to the refinement of CC, POD, CSI, FAR, RMSE, and BIAS via introducing more detailed information in the downscaling scheme.



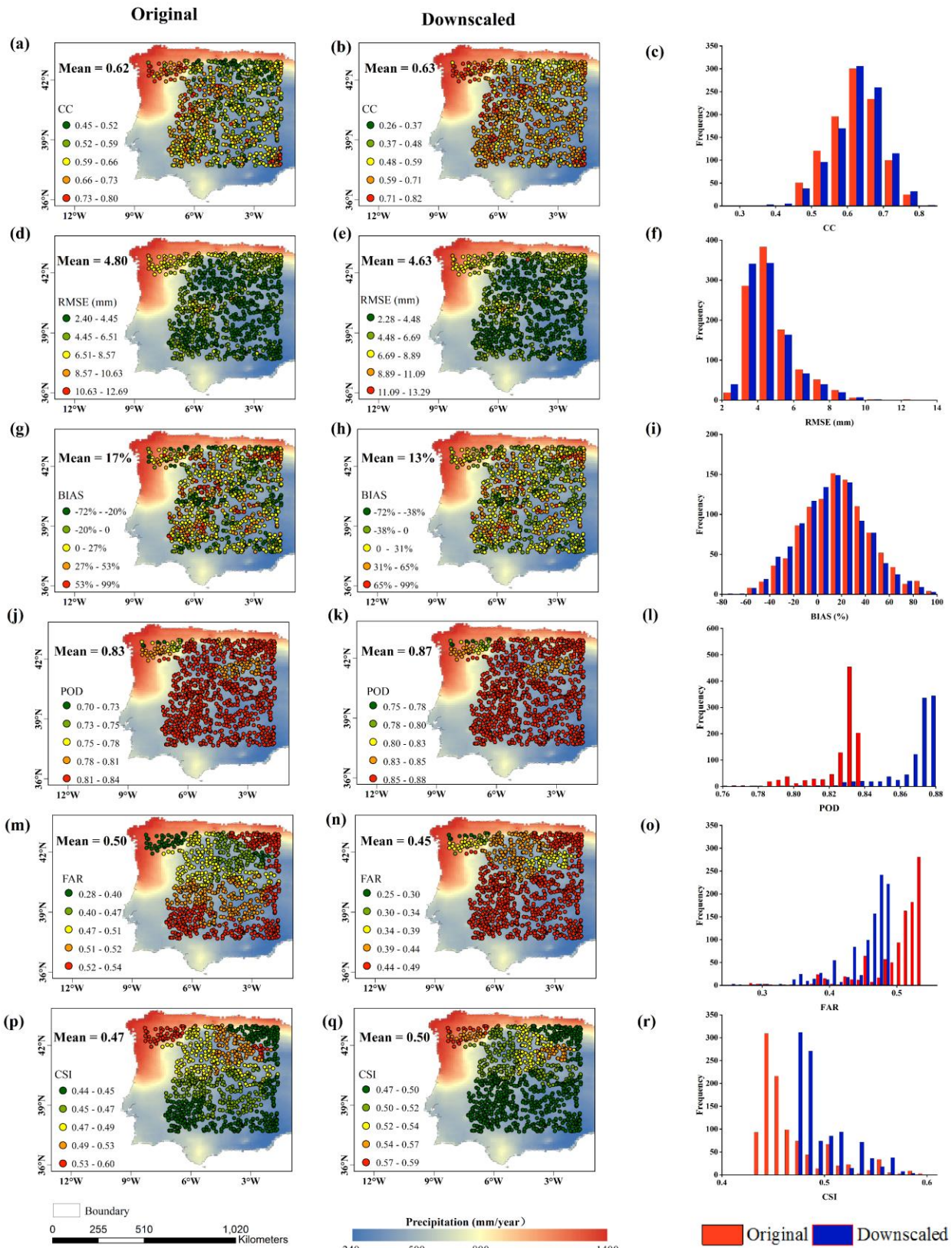
386 **Table 1.** Validation of the downscaled precipitation data, and original GPM precipitation data with the daily precipitation measured by the  
 387 selected stations at each month from 2016 to 2018.

Month	Original						Downscaled					
	CC	POD	FAR	CSI	RMSE (mm)	BIAS	CC	POD	FAR	CSI	RMSE (mm)	BIAS
January	0.57	0.84	0.49	0.47	6.36	14%	0.58	0.76	0.43	0.48	6.14	10%
February	0.56	0.86	0.49	0.47	6.83	7%	0.57	0.78	0.42	0.50	6.51	2%
March	0.66	0.89	0.45	0.52	6.27	-3%	0.66	0.83	0.40	0.54	6.10	-6%
April	0.60	0.89	0.45	0.51	5.67	9%	0.60	0.85	0.41	0.53	5.44	5%
May	0.60	0.90	0.46	0.50	4.78	5%	0.61	0.86	0.42	0.53	4.59	1%
June	0.55	0.90	0.48	0.49	3.31	15%	0.56	0.86	0.43	0.52	3.18	11%
July	0.63	0.90	0.49	0.48	2.72	24%	0.63	0.86	0.44	0.52	2.64	19%
August	0.61	0.90	0.50	0.48	2.05	14%	0.60	0.86	0.44	0.51	2.04	9%
September	0.50	0.90	0.51	0.47	2.74	34%	0.50	0.86	0.45	0.50	2.69	27%
October	0.57	0.89	0.51	0.46	4.34	12%	0.58	0.86	0.45	0.50	4.22	8%
November	0.59	0.89	0.50	0.47	6.18	10%	0.60	0.85	0.45	0.50	5.99	6%
December	0.59	0.88	0.51	0.46	5.66	14%	0.58	0.84	0.45	0.50	5.57	11%

388 **4.3.2 Spatial distribution of the daily validation at all in-situ measurements**

389 In addition to the general evaluation with the measurements from all stations, the downscaled results are separately  
 390 validated by the observations from each station, and the results are illustrated in Figure 8. In general, the downscaled  
 391 precipitation estimates produce less error than the original GPM precipitation products with respect to all overall error  
 392 statistics from 2016 to 2018, with an increase of CC values from 0.62 to 0.63, a decrease of RMSE values from 4.80 mm  
 393 to 4.63 mm, a decrease of BIAS values from 17% to 13%, a decrease of FAR values from 0.50 to 0.45, an increase of  
 394 POD values from 0.83 to 0.87 and an increase of CSI values from 0.47 to 0.50, respectively, which show moderate  
 395 improvement compared to that of the original GPM products. Moreover, from the frequency histogram of validation  
 396 indicators at 1027 in-situ measurements, the downscaled results present a better correlation with rain gauge observations  
 397 with most of the CC values being above 0.71 in the central and north-western regions. Regarding RMSE values of  
 398 downscaled results in Figure 8f, the validation at 728 in-situ measurements derives a low RMSE value (lower than 5.01  
 399 mm) and these stations are mainly located in the central and south-eastern regions. In comparison, the validation with  
 400 high RMSE majorly occurred in the north-western regions due to the originally bigger annual mean precipitation. For  
 401 BIAS, there is a relatively wide range from -72% to 99% in the whole region, systematic overestimation is observed at  
 402 685 stations, and underestimation is also observed at 342 stations. After downscaling, the overestimation was lightened.  
 403 About the rainfall event assessment, most of the CSI values are higher than 0.48 at these stations and the FAR values  
 404 are generally lower than 0.46, the POD values are generally higher than 0.81, as shown in Figure 8 j-r. It can also be  
 405 seen that the detection accuracy of precipitation events in the humid northern region is better than that in the southern

406 region with less precipitation. Those results indicate that the fitting relationship between observed precipitation and  
407 downscaled GPM products is good in the northwest region, while the errors in precipitation volumes are large in north-  
408 western regions due to rich precipitation, which is consistent with the performance of the original GPM precipitation  
409 product, while the accuracy was slightly better than that of the original precipitation product in the central and  
410 southeastern regions. It proves that the improvement in rainfall events introduced by the downscaling method is not  
411 limited to specific locations and covers the whole area, the downscaled results are more accurate in describing spatial  
412 precipitation details.



413  
 414 **Figure 8. CC (a-c), RMSE (d-f), BIAS (g-i), FAR (j-l), CSI (m-o) and corresponding frequency distributions for daily precipitation**  
 415 **of original and downscaled GPM precipitation estimates at 1027 in-situ measurements during 2016–2018. The background value**  
 416 **represents the original GPM annual average precipitation value from 2016 to 2018.**

417 Generally, the improvement from the overall performance for the downscaled results in Figure 8 is attributed to the  
 418 number of improvements in the validation site indicators that occur between the original GPM product, the downscaled

419 results, and the observation stations at the daily scale. The downscaled results outperformed the original product in the  
 420 detection accuracy of rainfall events and precipitation volumes, and the numbers of improvements in CSI and FAR are  
 421 1008 and 1026, respectively. Similarly, the number of improvements of CC, RMSE, and BIAS are 765, 886, and 884,  
 422 respectively. The downscaled results are more accurate than the original product when they are validated by field  
 423 measurements at most stations. In summary, the improvement in the precipitation downscaled by the SMPD method  
 424 occurs at most rain gauge stations. The evaluation demonstrates the ability of this method to increase spatial  
 425 heterogeneity to enhance the correlation with field measurements while also retaining the original GPM spatial  
 426 distribution pattern. All the above results clearly prove the effectiveness of the downscaling method, which enhances  
 427 daily GPM precipitation in both spatial information and accuracy.

### 428 4.3.3 Evaluation of precipitation intensities

429 To assess the downscaled GPM products' performance at different precipitation intensity intervals. The daily  
 430 precipitation intensity is classified into five categories based on the rainfall thresholds (0, 10, 20, and 40 mm) Zambrano-  
 431 Bigiarini et al. (2017). The performance metrics for the five daily precipitation intensity classes from 2016 to 2018 for  
 432 1027 in-situ measurements are listed in Table 2. In summary, original and downscaled GPM products performed the best  
 433 in terms of all performance metrics for the no-rain events, while performing the worst for the violent rain events ( $> 40$   
 434  $\text{mm d}^{-1}$ ). All precipitation products indicated that FAR values continuously performed the worst for the violent rain  
 435 intensities, which showed that the products are still unable to accurately capture high precipitation values. Due to the  
 436 reduced FAR values, the CSI value performed the best for no-rain events, followed by the light rain ( $[0, 10) \text{ mm d}^{-1}$ ),  
 437 moderate rain ( $[10, 20) \text{ mm d}^{-1}$ ), heavy rain ( $[20, 40) \text{ mm d}^{-1}$ ) and violent rain events ( $> 40 \text{ mm d}^{-1}$ ), respectively.  
 438 Additionally, the BIAS values showed that all precipitation products overestimated the number of light rain and  
 439 underestimated moderate rain, heavy rain, and violent rain events. Most importantly, the performance of the downscaled  
 440 precipitation product was slightly better than the original precipitation product for different rainfall intensity events in  
 441 terms of CC, RMSE, POD, FAR and CSI values, indicating the reliability and accuracy of the downscaled products in  
 442 capturing different rainfall intensity events than the original precipitation products.

443 **Table 2** CC, RMSE, BIAS, POD, FAR and CSI values for the different precipitation intensities for original and  
 444 downscaled GPM products from 2016 to 2018 for 1027 rain gauge stations.

Intensity (mm/d)	Original						Downscaled					
	CC	RMSE (mm)	BIAS (%)	POD	FAR	CSI	CC	RMSE (mm)	BIAS (%)	POD	FAR	CSI
0	-	1.83	-	0.93	0.34	0.63	-	1.73	-	0.94	0.26	0.70

0-10	0.30	6.39	27.00	0.69	0.65	0.31	0.30	5.98	23.00	0.73	0.60	0.34
10-20	0.15	11.85	-20.00	0.26	0.75	0.15	0.15	11.50	-22.00	0.25	0.74	0.15
20-40	0.15	18.41	-33.00	0.25	0.78	0.13	0.14	18.31	-36.00	0.26	0.77	0.14
>40	0.28	39.53	-47.00	0.23	0.84	0.11	0.28	39.33	-50.00	0.25	0.82	0.12

#### 4.3.4 Validation at the monthly scale

In addition to the validation at the daily scale, the downscaling results were further evaluated at the monthly scale by integrating the daily results into the monthly amount. Figure 8 shows the multiannual average maps of the monthly precipitation from 2016 to 2018, including the original GPM product and the downscaled results. Similar to the daily comparison, the monthly distributions of both datasets have quite similar patterns over different months. The northern part of the study area has more precipitation than the southern part. The downscaled results maintain the precipitation centers in each month and depict the distributions around the centers well. The downscaled results can provide more detailed information regarding spatial distribution.

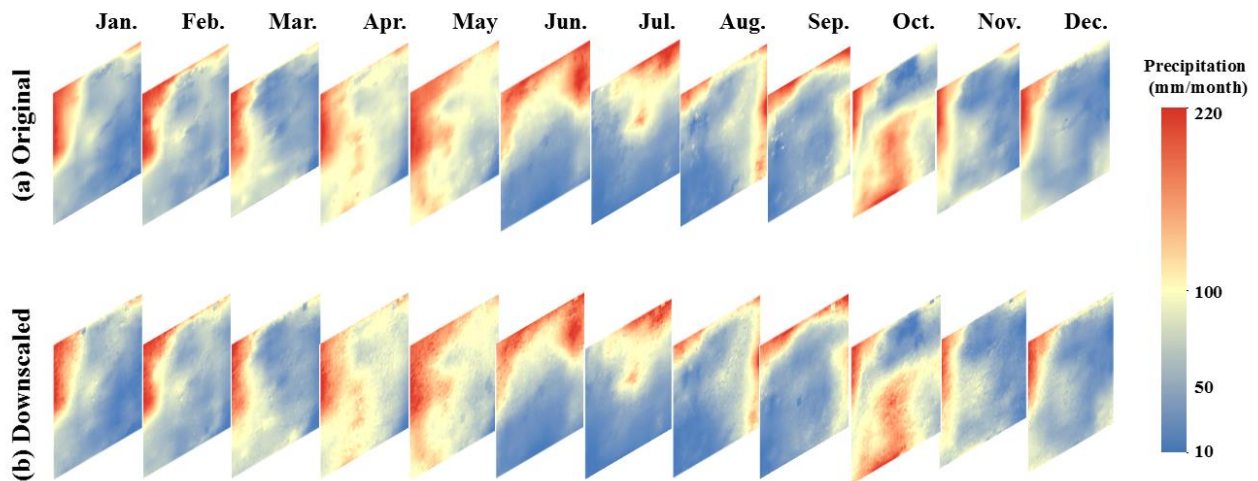
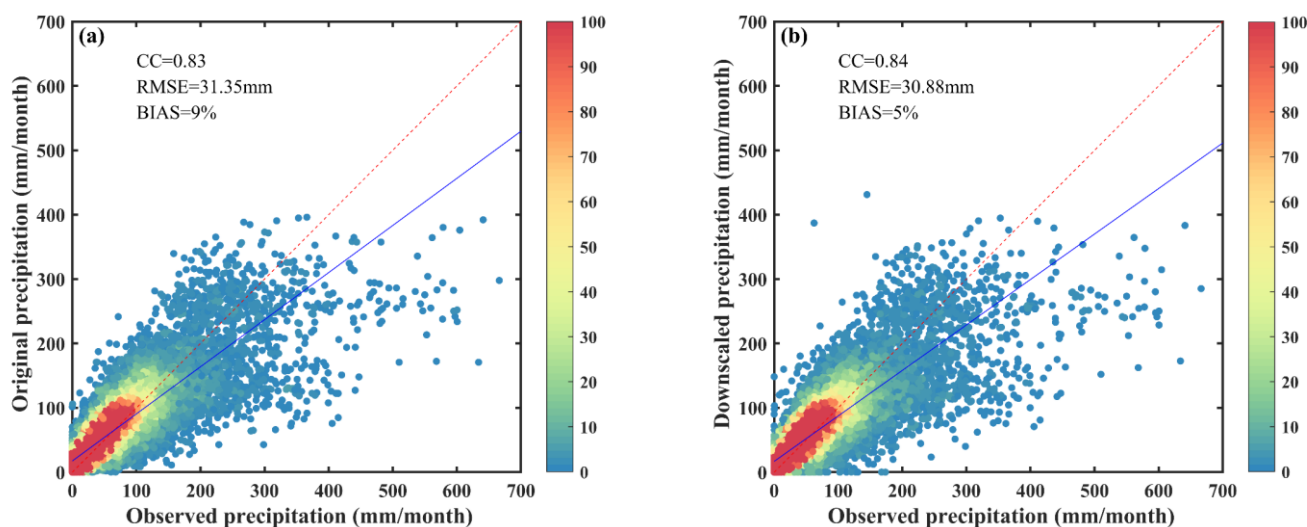


Figure 9. Spatial distribution of the multiannual mean value of monthly precipitation for the original GPM product (first line) and the downscaled results (second line) from 2016 to 2018.

By collecting the monthly precipitation of 1027 stations from 2016 to 2018, the accuracy of the monthly precipitation from the original and downscaled data was further quantitatively assessed. As shown in Figure 10a, after temporal integration, the uncertainty in the daily observation was greatly reduced in the monthly precipitation of the original GPM product. There is a significant increase in CC from 0.60 in Figure 6a to 0.83 in Figure 9a. However, systematic overestimation still occurs. After spatial downscaling, although there is no big change in terms of CC, both the RMSE and BIAS are clearly improved based on a comparison of the density plots in Figures 9a and b. For the analysis of the improvement ratio, only the performances of CC, RMSE, and BIAS are analyzed because the POD, FAR and CSI mainly reflect the rainfall events on the daily scale. Among the 1027 stations, the numbers of stations with improvements

464 during the validation in terms of CC, RMSE, and BIAS are 734, 587, and 912, respectively. Combined with the overall  
465 validation and individual validation, the downscaled results at the monthly scale outperformed the original GPM product.  
466 The evaluation shows that the downscaling method also presents good accuracy in the downscaling results and high  
467 robustness at the monthly scale.



468  
469 **Figure 10. Scatterplots of the original GPM precipitation product (a) and the downscaled precipitation data (b) plotted against the**  
470 **monthly precipitation measured by the meteorological stations during the period from 2016 to 2018.**

## 471 5 Discussion

472 In this study, a spatial downscaling method for coarse-resolution precipitation products was proposed to produce  
473 high-spatial resolution precipitation data at a 1 km scale with the use of 1 km SSM data downsampled from microwave  
474 remote sensing estimations. To establish the connection between SSM and precipitation, a simplified precipitation  
475 estimation model based on the surface water balance equation was developed with inspiration from the SM2RAIN model  
476 proposed by Brocca et al. (2014). By calibrating the model coefficients with a self-adaptive window at the coarse-  
477 resolution scale, the precipitation model was applied to high-resolution variables to obtain the high-resolution estimates.  
478 Compared with previous downscaling methods that mainly establish empirical relationships with surface variables, such  
479 as NDVI and topographic factors, this method introduces the physical relationship between SSM and precipitation via  
480 the water balance equation and has a solid physical basis. Therefore, the validation analysis conducted at both daily and  
481 monthly scales indicated that the downscaled precipitation data outperformed the original precipitation product in most  
482 circumstances and presented high robustness over three years with different rainfall strengthens.

### 483 5.1 Advantages of the downscaling method

484 In general, the SMPD method adopted the bottom-up approach in precipitation estimation, in which the variations  
485 in SSM sensed by microwave satellite sensors have a strong connection with rainfall amounts according to the principle



486 of water balance (Brocca et al., 2014; Brocca et al., 2016; Mao et al., 2018). After a sudden increase in soil moisture  
487 induced by rainfall events, the moisture condition gradually becomes drier when there is no further rainfall. Therefore,  
488 this method has a clear physical mechanism and is the only downscaling method using SSM as the key driving factor.  
489 Comparatively, the traditional statistical downscaling methods were established based on the statistical relationship  
490 between environmental factors and precipitation. Take the spatial interpolation method as an example, although the  
491 application of this method is convenient, the accuracy of the interpolated precipitation data is limited by the rainfall  
492 gauge density, especially in the mountainous watershed with complex topography (Zhang et al., 2020b; Guo et al., 2021).  
493 The high dependency on in-situ measurements constrains its applications in the area with few observations. In contrast,  
494 the SMPD method breaks the limitation caused by the rainfall gauge density and has a broader application prospect.

495 To further demonstrate the advantage of the SMPD method, it is beneficial to compare the validation accuracy of  
496 this method with the validation accuracies of existing downscaled approaches, as shown in Table 3. In current existing  
497 downscaling studies, the involvement of daily SSM ensures downscaling at a daily scale is rarely considered. However,  
498 the relationship between SSM and precipitation ensures the daily downscaling in the proposed SMPD method.  
499 Comparatively, although Yan et al. (2021) conducted daily precipitation downscaling with the use of the random forest  
500 (RF) method, the RMSE value was considerably lower than that of the SMPD method. Moreover, this machine-learning  
501 method is highly dependent on the available training dataset. Comparatively, the daily or sub-daily downscaling studies  
502 conducted by Long et al. (2016) and Chao et al. (2018) have relatively better performances in terms of RMSE and CC,  
503 respectively. However, the incorporation of gauge precipitation data in the downscaling process partly enhances the  
504 estimation accuracy. These methods highly rely on in situ measurements without the independence of rain gauge  
505 measurements. In a recent hour-scale downscaling study conducted by Ma et al. (2020a), a geographically moving  
506 window weight disaggregation analysis (GMWWDA) method was developed by introducing cloud properties as  
507 covariates to downscale GPM precipitation products. Although it provided estimates at a very high temporal frequency,  
508 the limited rainfall-related environmental variables at the 0.01°/hourly scale constrained its application.

509 For the intercomparison of the monthly accuracy, the daily downscaled results of the proposed method  
510 outperformed most of the previous monthly downscaling studies using either RF or GWR algorithms (Jia et al., 2011;  
511 Xu et al., 2015; Jing et al., 2016b; Chen et al., 2018; Zhan et al., 2018). As shown in Figure 9b, the CC value was higher  
512 than most of them in the abovementioned studies. Although the RF-based downscaling method in Jing et al. (2016b) has  
513 a relatively low RMSE, the measurements from in situ stations were used to train the downscaling model which greatly  
514 reduces the dependence of the downscaling process on field observations. A similar requirement is also presented in Lu  
515 et al. (2019) and Long et al. (2016), and the GWR and multivariate regression models are largely dependent on the  
516 number of available training stations and variables related to the geophysical mechanisms of precipitation. The

517 independence of field observations in the SMPD method shows a large advantage, especially for regions with sparse  
518 meteorological stations. Zeng et al. (2021) also proposed an independent downscaling approach considering temporal  
519 lag from vegetation changes to precipitation. However, the relationship shows high variability which may result in a  
520 negative correlation within a short time. Therefore, both the CC and RMSE of this method have worse performances  
521 than those of the proposed method. In general, according to the methodology comparison, the proposed SMPD method  
522 exhibits good performance in terms of both CC and RMSE. Unlike using the empirical regression method to build the  
523 relationship between precipitation and other surface variables, the SMPD method demonstrated high effectiveness,  
524 independence, and robustness.



525 **Table 3.** List of the performance of downscaling procedures to improve the spatial resolution of satellite precipitation products at different temporal scales. The bold  
 526 letters represent the proposed method in this study.

Original products	Downscaled algorithm	Auxiliary variables	Temporal resolution	Downscaled products			Reference
				Spatial resolution	CC	RMSE (mm)	
TRMM (25 km)	RF	DEM, NDVI	Monthly	1 km	0.86	15.70	Jing et al. (2016b)
GPM (10 km)	GWR	DEM, NDVI	Monthly	1 km	0.79	20.94	Lu et al. (2019)
GPM (10 km)	GWR	DEM, NDVI	Monthly	1 km	0.79	27.23	Zhan et al. (2018)
TRMM (25 km)	GWR	DEM, Rain gauge data	Monthly	1 km	0.87	46.14	Chen et al. (2018)
TRMM (25 km)	GWR	DEM, NDVI	Monthly	1 km	0.82	25.10	Xu et al. (2015)
GPM (10 km)	RF	DEM, NDVI, LST	Daily	1 km	0.64	6.06	Yan et al. (2021)
TRMM (25 km)	Multivariate regression model	DEM, Climate data	Daily	1 km	-	2.71	Long et al. (2016)
GPM (10 km)	LPVIAL	NDVI	16-day	1 km	0.81	46.77	Zeng et al. (2021)
CMORPH (8 km)	GWR	DEM, NDVI	30 min	1 km	0.86	7.27	Chao et al. (2018)
GPM (10 km)	AMCN, GDA	LST, EVI, LSR	Monthly	1 km	0.83	30.88	Jing et al. (2022)
GPM (10 km)	GMWWDA	Cloud Property Data	Hourly	1 km	0.53	5.16	Ma et al. (2020a)
GPM (10 km)	SVM	Atmospheric, variables, DEM	Daily	1 km	0.78	12.55	Min et al. (2020)
<b>GPM (10 km)</b>	<b>SMPD</b>	<b>SSM, NDVI</b>	<b>Daily</b>	<b>1 km</b>	<b>0.61</b>	<b>4.83</b>	<b>Proposed method</b>

## 528 5.2 Limitations and prospects

529 Despite the superior performance of the SMPD method, some issues still need to be considered in practical  
530 applications. The first issue should relate to the accuracy of the original GPM precipitation data. Due to the limitation of  
531 the inherent accuracy of original GPM precipitation data, which are mainly manifested in two aspects, firstly the IMERG-  
532 Final products are corrected on a monthly scale using the interpolated precipitation product Global Precipitation  
533 Climatology Centre (GPCC, 1.0°/Monthly) based on ground observations. However, there is no mature calibration  
534 algorithm for calibrating the daily satellite-based precipitation estimates (Ma et al., 2020b). Second, the prior databases  
535 of cloud cover and precipitation profiles for retrieving passive microwave-based satellite precipitation estimates are not  
536 sufficiently robust due to the lack of ground-based radar observations. In addition, since passive microwave remote  
537 sensing-based precipitation retrieval is the primary input to the IMERG-Final products, it may lead to poor performance  
538 of the satellite-based product in winter and high-latitude regions (Xu et al., 2022). Therefore, the improvement in the  
539 accuracy of downscaling results is limited because of the value preservation during the downscaling process. The  
540 downscaling performance is highly dependent on the accuracy of the original GPM products. The multisource data fusion  
541 model based on observed rain gauge stations and reanalysis data proposed by Ma et al. (2021) and Li and Long (2020)  
542 could increase its ability to describe the daily precipitation fluctuations and it would help provide more accurate  
543 downscaling precipitation values. Given the spatial inconsistency of the point measurement and grid-scale estimation,  
544 which may lead to some uncertainty in the evaluation results. Thus, the difference in spatial scale between satellite and  
545 gauge-based precipitation measurements should be paid more attention to in future comparisons based on reanalysis-  
546 based precipitation with high spatial resolution.

547 In addition, the uncertainty of SSM and the sensitivity relationship between SSM and precipitation under continuous  
548 rainfall conditions may introduce uncertainty in the downscaling precipitation results. First, the responses of SSM with  
549 different land cover conditions and vegetation coverages to precipitation are relatively different (Fan et al., 2021), and  
550 topographic factors such as depressions and slopes also affect the uncertainty of SSM. Therefore, it is necessary to  
551 establish the relationship between SSM and precipitation for different land cover types or different terrain types. The  
552 establishment of a more reliable fitting relationship based on precipitation data with different land cover properties or  
553 topographic factors would be helpful to enhance the accuracy of the downscaling results (Chen et al., 2020; Senanayake  
554 et al., 2021; Zhao et al., 2021). Second, although the relationship between SSM and precipitation has been well  
555 demonstrated in many previous studies, the sensitivity of SSM to precipitation may decrease when soil water storage  
556 becomes saturated after repeated precipitation (Song et al., 2020). Therefore, it is necessary to further improve the  
557 relationship by considering the soil water threshold saturation in future studies. Moreover, this downscaling method was  
558 based on the surface water balance principle, and the runoff factor under heavy precipitation conditions at a certain time

559 was not considered because of the inherent scarcity of high-resolution runoff datasets from in situ measurements. Some  
560 studies have provided good alternatives to obtain runoff data with high spatiotemporal resolution (Jadidoleslam et al.,  
561 2019; Muelchi et al., 2021). Hence, the use of this runoff factor in the water balance equation for heavy precipitation  
562 will assist in improving downscaling accuracy.

563 Most importantly, many previous studies have successfully generated fine precipitation data at hourly or half-hourly  
564 scales (Ma et al., 2020a; Ma et al., 2020b; Lu et al., 2022; Ma et al., 2022). Nevertheless, these studies lacked physical  
565 mechanisms in the downscaling process and do not use surface soil moisture covariates that respond in real-time to  
566 precipitation. In the proposed method, the key inputs of the downscaling process are surface soil moisture and  
567 precipitation data. Even on hourly or half-hourly scales, the soil moisture exhibits an instantaneous response to collocated  
568 precipitation. Then, the soil moisture estimation method achieved seamless downscaling for high-resolution soil moisture  
569 generation under cloudy conditions. Therefore, it would be able to obtain real-time soil moisture from microwave  
570 satellite observations combined with surface temperature and vegetation index derived from optical and thermal infrared  
571 remote sensing. Therefore, this approach has the potential for generating high spatial resolution precipitation data at  
572 hourly or half-hourly scale.

## 573 **6 Conclusions**

574 In this paper, by introducing high-resolution SSM data and the NDVI as independent variables, a novel physical  
575 downscaling approach based on the principle of surface water balance is developed to obtain high-resolution ( $1 \text{ km} \times 1$   
576 km) daily precipitation estimation. At both daily and monthly scales, the downscaled precipitation presents a similar  
577 spatial and temporal distribution pattern as the original GPM product. Furthermore, a systematic evaluation of the  
578 downscaled GPM data was conducted on multiple time scales at the station level. The downscaled precipitation showed  
579 a good correlation with the observed measurements at each station at the daily scale, with POD, FAR, CSI, CC, RMSE,  
580 and BIAS values of 0.88, 0.47, 0.48, 0.61, 4.83 mm, and 5%, respectively, and the evaluation results outperformed the  
581 original GPM product. For monthly scale comparison, the downscaled data also presented a strong correlation with the  
582 observed precipitation, with CC, RMSE, and BIAS values of 0.84, 30.88 mm, and 5%, respectively. With the increase  
583 in spatial heterogeneity in the downscaled results, there is also an increasing trend in the improvements in the  
584 precipitation accuracy through the comparison at most stations.

585 In summary, the proposed method with the use of surface water balance principle has a more solid physical basis  
586 than previous downscaling methods. By introducing SSM as an auxiliary variable, the impact of inherent bias in satellite  
587 estimates on the downscaled results can be moderately reduced compared to the conventional statistical method. The  
588 validation with rain gauge data highlights the importance of SSM as a fully independent source of information that can

589 be effectively used for downscaling coarse-resolution precipitation at a daily scale, which is rarely conducted in current  
590 related studies. Therefore, this method is a promising way to derive high-resolution precipitation data and shows good  
591 potential for real-time precipitation data downscaling with the provision of SSM data, which will assist further  
592 applications in related fields (such as hydrology, agriculture, natural hazards, water resources, and climate change).

### 593 **Code and data availability**

594 This study used the surface soil moisture data with high resolution (<https://doi.org/10.5281/zenodo.7451422>) to  
595 produce the downscaled precipitation data (<https://doi.org/10.5281/zenodo.7451690>), which were available at the zenodo  
596 data survey portal. The part of observed data obtained on ([https://www.ncei.noaa.gov/access/search/data-search/global-](https://www.ncei.noaa.gov/access/search/data-search/global-summary-of-the-day)  
597 [summary-of-the-day](https://www.ncei.noaa.gov/access/search/data-search/global-summary-of-the-day)). The Matlab codes can be obtained upon request from the corresponding author.

### 598 **Author contributions**

599 Kunlong He led the investigation, conceptualized the study, designed the formal analysis, and wrote the initial draft. Wei  
600 Zhao was responsible for conceptualizing the study, investigating methods, obtaining the funding, supervising the study  
601 process, and reviewing and editing the paper. Luca Brocca conceptualized the research, reviewed the manuscript and  
602 provided the in-situ measurements. Pere Quintana-Seguí helped with the investigation, provided the datasets, and  
603 reviewed the paper.

### 604 **Declaration of Competing Interest**

605 The authors declare that they have no known competing financial interests or personal relationships that could have  
606 appeared to influence the work reported in this paper.

### 607 **Acknowledgments**

608 This research was partially funded as part of the National Natural Science Foundation of China (Grant No. 42071349),  
609 Sichuan Science and Technology Program (Grant No. 2020JDJQ0003), the West Light Foundation of the Chinese  
610 Academy of Sciences, and the project PRIMA PCI2020-112043 funded by MCIN/AEI/10.13039/501100011033. We  
611 thank the Spanish State Meteorological Agency (AEMET) for sharing daily precipitation data with this project.

### 612 **Review statement**

613 The authors sincerely thank Editor Shraddhanand Shukla and three anonymous referees for their insightful comments.

- 615 Abdollahipour, A., Ahmadi, H., and Aminnejad, B.: A review of downscaling methods of satellite-based precipitation  
616 estimates, *Earth. Sci. Inform.*, 1-20, <https://doi.org/10.1007/s12145-021-00669-4>, 2021.
- 617 Baez-Villanueva, O. M., Zambrano-Bigiarini, M., Beck, H. E., McNamara, I., Ribbe, L., Nauditt, A., Birkel, C., Verbist,  
618 K., Giraldo-Osorio, J. D., and Tinh, N. X.: RF-MEP: A novel Random Forest method for merging gridded precipitation  
619 products and ground-based measurements, *Remote Sens. Environ.*, 239, 111606,  
620 <https://doi.org/10.1016/j.rse.2019.111606>, 2020.
- 621 Bezak, N., Borrelli, P., and Panagos, P.: Exploring the possible role of satellite-based rainfall data in estimating inter-  
622 and intra-annual global rainfall erosivity, *Hydrol. Earth Syst. Sci.*, 26, 1907–1924, <https://doi.org/10.5194/hess-26-1907-2022>, 2022.
- 623 Birtwistle, A. N., Laituri, M., Bledsoe, B., and Friedman, J. M.: Using NDVI to measure precipitation in semi-arid  
624 landscapes, *Journal of Arid Environments*, 131, 15-24, <https://doi.org/10.1016/j.jaridenv.2016.04.004>, 2016.
- 625 Brocca, L., Moramarco, T., Melone, F., and Wagner, W.: A new method for rainfall estimation through soil moisture  
626 observations, *Geophys. Res. Lett.*, 40, 853-858, <https://doi.org/10.1002/grl.50173>, 2013.
- 627 Brocca, L., Filippucci, P., Hahn, S., Ciabatta, L., Massari, C., Camici, S., Schüller, L., Bojkov, B., and Wagner, W.:  
628 SM2RAIN–ASCAT (2007–2018): global daily satellite rainfall data from ASCAT soil moisture observations, *Earth Syst.*  
629 *Sci. Data.*, 11, 1583–1601, <https://doi.org/10.5194/essd-11-1583-2019>, 2019.
- 630 Brocca, L., Pellarin, T., Crow, W. T., Ciabatta, L., Massari, C., Ryu, D., Su, C. H., Rüdiger, C., and Kerr, Y.: Rainfall  
631 estimation by inverting SMOS soil moisture estimates: A comparison of different methods over Australia, *J. Geophys.*  
632 *Res. - Atmos.*, 121, 12,062-012,079, <https://doi.org/10.1002/2016JD025382>, 2016.
- 633 Brocca, L., Ciabatta, L., Massari, C., Moramarco, T., Hahn, S., Hasenauer, S., Kidd, R., Dorigo, W., Wagner, W., and  
634 Levizzani, V.: Soil as a natural rain gauge: Estimating global rainfall from satellite soil moisture data, *J. Geophys. Res.*  
635 *- Atmos.*, 119, 5128-5141, <https://doi.org/10.1002/2014JD021489>, 2014.
- 636 Brocca, L., Massari, C., Ciabatta, L., Moramarco, T., Penna, D., Zuecco, G., Pianezzola, L., Borga, M., Matgen, P., and  
637 Martínez-Fernández, J.: Rainfall estimation from in situ soil moisture observations at several sites in Europe: an  
638 evaluation of the SM2RAIN algorithm, *J. Hydrol. Hydromech.*, 63, 201-209, <https://doi.org/10.1515/johh-2015-0016>,  
639 2015.
- 640 Carpintero, E., Mateos, L., Andreu, A., and González-Dugo, M. P.: Effect of the differences in spectral response of  
641 Mediterranean tree canopies on the estimation of evapotranspiration using vegetation index-based crop coefficients, *Agr.*  
642 *Water Manage.*, 238, 106201, <https://doi.org/10.1016/j.agwat.2020.106201>, 2020.
- 643 Chao, L., Zhang, K., Li, Z., Zhu, Y., Wang, J., and Yu, Z.: Geographically weighted regression based methods for  
644 merging satellite and gauge precipitation, *J. Hydrol.*, 558, 275-289, <https://doi.org/10.1016/j.jhydrol.2018.01.042>, 2018.
- 645 Chen, F., Crow, W., and Holmes, T. R.: Improving long-term, retrospective precipitation datasets using satellite-based  
646 surface soil moisture retrievals and the soil moisture analysis rainfall tool, *J. Appl. Remote. Sens.*, 6, 063604,  
647 <https://doi.org/10.1117/1.JRS.6.063604>, 2012.
- 648 Chen, S., Xiong, L., Ma, Q., Kim, J.-S., Chen, J., and Xu, C.-Y.: Improving daily spatial precipitation estimates by  
649 merging gauge observation with multiple satellite-based precipitation products based on the geographically weighted  
650 ridge regression method, *J. Hydrol.*, 589, 125156, <https://doi.org/10.1016/j.jhydrol.2020.125156>, 2020.
- 651 Chen, Y., Huang, J., Sheng, S., Mansaray, L. R., Liu, Z., Wu, H., and Wang, X.: A new downscaling-integration  
652 framework for high-resolution monthly precipitation estimates: Combining rain gauge observations, satellite-derived  
653 precipitation data and geographical ancillary data, *Remote Sens. Environ.*, 214, 154-172,  
654 <https://doi.org/10.1016/j.rse.2018.05.021>, 2018.
- 655 Ciabatta, L., Marra, A. C., Panegrossi, G., Casella, D., Sandò, P., Dietrich, S., Massari, C., and Brocca, L.: Daily  
656 precipitation estimation through different microwave sensors: Verification study over Italy, *J. Hydrol.*, 545, 436-450,  
657 <https://doi.org/10.1016/j.jhydrol.2016.12.057>, 2017.

659 Ciabatta, L., Massari, C., Brocca, L., Gruber, A., Reimer, C., Hahn, S., Paulik, C., Dorigo, W., Kidd, R., and Wagner,  
660 W.: SM2RAIN-CCI: a new global long-term rainfall data set derived from ESA CCI soil moisture, *Earth Syst. Sci. Data.*,  
661 10, 267–280, <https://doi.org/10.5194/essd-10-267-2018>, 2018.

662 Colliander, A., Jackson, T. J., Bindlish, R., Chan, S., Das, N., Kim, S., Cosh, M., Dunbar, R., Dang, L., and Pashaian,  
663 L.: Validation of SMAP surface soil moisture products with core validation sites, *Remote Sens. Environ.*, 191, 215-231,  
664 <https://doi.org/10.1016/j.rse.2017.01.021>, 2017.

665 Dorigo, W., Wagner, W., Albergel, C., Albrecht, F., Balsamo, G., Brocca, L., Chung, D., Ertl, M., Forkel, M., Gruber,  
666 A., Haas, E., Hamer, P. D., Hirschi, M., Ikonen, J., de Jeu, R., Kidd, R., Lahoz, W., Liu, Y. Y., Miralles, D., Mistelbauer,  
667 T., Nicolai-Shaw, N., Parinussa, R., Pratola, C., Reimer, C., van der Schalie, R., Seneviratne, S. I., Smolander, T., and  
668 Lecomte, P.: ESA CCI Soil Moisture for improved Earth system understanding: State-of-the art and future directions,  
669 *Remote Sens. Environ.*, 203, 185-215, <https://doi.org/10.1016/j.rse.2017.07.001>, 2017.

670 Duan, Z. and Bastiaanssen, W.: First results from Version 7 TRMM 3B43 precipitation product in combination with a  
671 new downscaling–calibration procedure, *Remote Sens. Environ.*, 131, 1-13, <https://doi.org/10.1016/j.rse.2012.12.002>,  
672 2013.

673 Ebrahimi, H. and Azadbakht, M.: Downscaling MODIS land surface temperature over a heterogeneous area: An  
674 investigation of machine learning techniques, feature selection, and impacts of mixed pixels, *Comput Geosci-UK.*, 124,  
675 93-102, <https://doi.org/10.1016/j.cageo.2019.01.004>, 2019.

676 Famiglietti, J. S. and Wood, E. F.: Multiscale modeling of spatially variable water and energy balance processes, *Water*  
677 *Resour. Res.*, 30, 3061-3078, <https://doi.org/10.1029/94WR01498>, 1994.

678 Fan, Y., Ma, Z., Ma, Y., Ma, W., Xie, Z., Ding, L., Han, Y., Hu, W., and Su, R.: Respective Advantages of “Top-Down”  
679 Based GPM IMERG and “Bottom-Up” Based SM2RAIN-ASCAT Precipitation Products Over the Tibetan Plateau, *J.*  
680 *Geophys. Res. - Atmos.*, 126, e2020JD033946, <https://doi.org/10.1029/2020JD033946>, 2021.

681 Gruber, A., Scanlon, T., van der Schalie, R., Wagner, W., and Dorigo, W.: Evolution of the ESA CCI Soil Moisture  
682 climate data records and their underlying merging methodology, *Earth Syst. Sci. Data*, 11, 717–739,  
683 <https://doi.org/10.5194/essd-11-717-2019>, 2019.

684 Guo, X., Guo, Cui, P., Chen, X., Li, Y., Zhang, J., and Sun, Y.: Spatial uncertainty of rainfall and its impact on  
685 hydrological hazard forecasting in a small semiarid mountainous watershed, *J. Hydrol.*, 595, 126049,  
686 <https://doi.org/10.1016/j.jhydrol.2021.126049>, 2021.

687 Haylock, M. R., Cawley, G. C., Harpham, C., Wilby, R. L., and Goodess, C. M.: Downscaling heavy precipitation over  
688 the United Kingdom: a comparison of dynamical and statistical methods and their future scenarios, *Int J Climatol: A*  
689 *Journal of the Royal Meteorological Society*, 26, 1397-1415, <https://doi.org/10.1002/joc.1318>, 2006.

690 He, X., Chaney, N. W., Schleiss, M., and Sheffield, J.: Spatial downscaling of precipitation using adaptable random  
691 forests, *Water Resour. Res.*, 52, 8217-8237, <https://doi.org/10.1002/2016WR019034>, 2016.

692 Hong, Z., Han, Z., Li, X., Long, D., Tang, G., and Wang, J.: Generation of an improved precipitation dataset from  
693 multisource information over the Tibetan Plateau, *J. Hydrometeorol.*, 22, 1275-1295, [https://doi.org/10.1175/JHM-D-  
694 20-0252.1](https://doi.org/10.1175/JHM-D-20-0252.1), 2021.

695 Hou, A. Y., Kakar, R. K., Neeck, S., Azarbarzin, A. A., Kummerow, C. D., Kojima, M., Oki, R., Nakamura, K., and  
696 Iguchi, T.: The Global Precipitation Measurement Mission, *B. Am. Meteorol. Soc.*, 95, 701-722,  
697 <https://doi.org/10.1175/BAMS-D-13-00164.1>, 2014.

698 Huffman, G. J., Bolvin, D. T., Braithwaite, D., Hsu, K., Joyce, R., Xie, P., and Yoo, S.-H.: NASA global precipitation  
699 measurement (GPM) integrated multi-satellite retrievals for GPM (IMERG), Algorithm Theoretical Basis Document  
700 (ATBD) Version, 4, 26, 2015.

701 Huffman, G. J., Bolvin, D. T., Nelkin, E. J., Wolff, D. B., Adler, R. F., Gu, G., Hong, Y., Bowman, K. P., and Stocker,  
702 E. F.: The TRMM Multisatellite Precipitation Analysis (TMPA): Quasi-global, multiyear, combined-sensor precipitation  
703 estimates at fine scales, *J. Hydrometeorol.*, 8, 38-55, <https://doi.org/10.1175/JHM560.1>, 2007.

704 Huffman, G. J., Adler, R. F., Arkin, P., Chang, A., Ferraro, R., Gruber, A., Janowiak, J., McNab, A., Rudolf, B., and  
705 Schneider, U.: The global precipitation climatology project (GPCP) combined precipitation dataset, *B. Am. Meteorol.*  
706 *Soc.*, 78, 5-20, <https://doi.org/10.1175/1520-0477>, 1997.

707 Huffman, G. J., Bolvin, D. T., Braithwaite, D., Hsu, K.-L., Joyce, R. J., Kidd, C., Nelkin, E. J., Sorooshian, S., Stocker,  
708 E. F., and Tan, J.: Integrated multi-satellite retrievals for the Global Precipitation Measurement (GPM) mission (IMERG),  
709 in: *Satellite precipitation measurement*, Springer, Cham, 343-353, [https://doi.org/10.1007/978-3-030-24568-9\\_19](https://doi.org/10.1007/978-3-030-24568-9_19), 2020.

710 Hutengs, C. and Vohland, M.: Downscaling land surface temperatures at regional scales with random forest regression,  
711 *Remote Sens. Environ.*, 178, 127-141, <http://dx.doi.org/10.1016/j.rse.2016.03.006>, 2016.

712 Immerzeel, W. W., Rutten, M. M., and Droogers, P.: Spatial downscaling of TRMM precipitation using vegetative  
713 response on the Iberian Peninsula, *Remote Sens. Environ.*, 113, 362-370, <https://doi.org/10.1016/j.rse.2008.10.004>, 2009.

714 Jadidoleslam, N., Mantilla, R., Krajewski, W. F., and Goska, R.: Investigating the role of antecedent SMAP satellite soil  
715 moisture, radar rainfall and MODIS vegetation on runoff production in an agricultural region, *J. Hydrol.*, 579, 124210,  
716 <https://doi.org/10.1016/j.jhydrol.2019.124210>, 2019.

717 Jia, S., Zhu, W., Lü, A., and Yan, T.: A statistical spatial downscaling algorithm of TRMM precipitation based on NDVI  
718 and DEM in the Qaidam Basin of China, *Remote Sens. Environ.*, 115, 3069-3079,  
719 <https://doi.org/10.1016/j.rse.2011.06.009>, 2011.

720 Jing, W., Yang, Y., Yue, X., and Zhao, X.: A Spatial Downscaling Algorithm for Satellite-Based Precipitation over the  
721 Tibetan Plateau Based on NDVI, DEM, and Land Surface Temperature, *Remote Sens.*, 8, 655,  
722 <https://doi.org/10.3390/rs8080655>, 2016a.

723 Jing, W., Yang, Y., Yue, X., and Zhao, X.: A Comparison of Different Regression Algorithms for Downscaling Monthly  
724 Satellite-Based Precipitation over North China, *Remote Sens.*, 8, 1-17, <https://doi.org/10.3390/rs8100835>, 2016b.

725 Jing, Y., Lin, L., Li, X., Li, T., and Shen, H.: An attention mechanism based convolutional network for satellite  
726 precipitation downscaling over China, *J. Hydrol.*, 613, 128388, <https://doi.org/10.1016/j.jhydrol.2022.128388>, 2022.

727 Joiner, J., Yoshida, Y., Anderson, M., Holmes, T., Hain, C., Reichle, R., Koster, R., Middleton, E., and Zeng, F.-W.:  
728 Global relationships among traditional reflectance vegetation indices (NDVI and NDII), evapotranspiration (ET), and  
729 soil moisture variability on weekly timescales, *Remote Sens. Environ.*, 219, 339-352,  
730 <https://doi.org/10.1016/j.rse.2018.10.020>, 2018.

731 Joyce, R. J., Janowiak, J. E., Arkin, P. A., and Xie, P.: CMORPH: A method that produces global precipitation estimates  
732 from passive microwave and infrared data at high spatial and temporal resolution, *J. Hydrometeorol.*, 5, 487-503,  
733 <https://doi.org/10.1175/1525-7541>, 2004.

734 Kubota, T., Shige, S., Hashizume, H., Aonashi, K., Takahashi, N., Seto, S., Hirose, M., Takayabu, Y. N., Ushio, T., and  
735 Nakagawa, K.: Global precipitation map using satellite-borne microwave radiometers by the GSMaP project: Production  
736 and validation, *IEEE Trans. Geosci. Remote Sens.*, 45, 2259-2275, <https://doi.org/10.1109/TGRS.2007.895337>, 2007.

737 Li, X. and Long, D.: An improvement in accuracy and spatiotemporal continuity of the MODIS precipitable water vapor  
738 product based on a data fusion approach, *Remote Sens. Environ.*, 248, 111966, <https://doi.org/10.1016/j.rse.2020.111966>,  
739 2020.

740 Lin, A. and Wang, X. L.: An algorithm for blending multiple satellite precipitation estimates with in situ precipitation  
741 measurements in Canada, *J. Geophys. Res. - Atmos.*, 116, <https://doi.org/10.1029/2011JD016359>, 2011.

742 Long, D., Bai, L., Yan, L., Zhang, C., Yang, W., Lei, H., Quan, J., Meng, X., and Shi, C.: Generation of spatially  
743 complete and daily continuous surface soil moisture of high spatial resolution, *Remote Sens. Environ.*, 233, 111364,  
744 <https://doi.org/10.1016/j.rse.2019.111364>, 2019.

745 Long, Y., Zhang, Y., and Ma, Q.: A Merging Framework for Rainfall Estimation at High Spatiotemporal Resolution for  
746 Distributed Hydrological Modeling in a Data-Scarce Area, *Remote Sens.*, 8, 599, <https://doi.org/10.3390/rs8070599>,  
747 2016.

748 Lu, X., Chen, Y., Tang, G., Wang, X., Liu, Y., and Wei, M.: Quantitative estimation of hourly precipitation in the  
749 Tianshan Mountains based on area-to-point kriging downscaling and satellite-gauge data merging, *J. Mt. Sci.*, 19, 58-  
750 72, <https://doi.org/10.1007/s11629-021-6901-5>, 2022.



751 Lu, X., Tang, G., Wang, X., Liu, Y., Jia, L., Xie, G., Li, S., and Zhang, Y.: Correcting GPM IMERG precipitation data  
752 over the Tianshan Mountains in China, *J. Hydrol.*, 575, 1239-1252, <https://doi.org/10.1016/j.jhydrol.2019.06.019>, 2019.

753 Ma, Y., Sun, X., Chen, H., Hong, Y., and Zhang, Y.: A two-stage blending approach for merging multiple satellite  
754 precipitation estimates and rain gauge observations: an experiment in the northeastern Tibetan Plateau, *Hydrol. Earth  
755 Syst. Sci.*, 25, 359–374, <https://doi.org/10.5194/hess-25-359-2021>, 2021.

756 Ma, Z., Zhou, Y., Hu, B., Liang, Z., and Shi, Z.: Downscaling annual precipitation with TMPA and land surface  
757 characteristics in China, *Int. J. Climatol.*, 37, 5107-5119, <https://doi.org/10.1002/joc.5148>, 2017a.

758 Ma, Z., He, K., Tan, X., Liu, Y., Lu, H., and Shi, Z.: A new approach for obtaining precipitation estimates with a finer  
759 spatial resolution on a daily scale based on TMPA V7 data over the Tibetan Plateau, *Int. J. Remote Sens.*, 40, 8465-8483,  
760 <https://doi.org/10.1080/01431161.2019.1612118>, 2019a.

761 Ma, Z., Shi, Z., Zhou, Y., Xu, J., Yu, W., and Yang, Y.: A spatial data mining algorithm for downscaling TMPA 3B43  
762 V7 data over the Qinghai–Tibet Plateau with the effects of systematic anomalies removed, *Remote Sens. Environ.*, 200,  
763 378-395, <https://doi.org/10.1016/j.rse.2017.08.023>, 2017b.

764 Ma, Z., Ghent, D., Tan, X., He, K., Li, H., Han, X., Huang, Q., and Peng, J.: Long-Term Precipitation Estimates  
765 Generated by a Downscaling-Calibration Procedure Over the Tibetan Plateau From 1983 to 2015, *Earth Space Sci.*, 6,  
766 2180-2199, <https://doi.org/10.1029/2019EA00065>, 2019b.

767 Ma, Z., Xu, J., He, K., Han, X., Ji, Q., Wang, T., Xiong, W., and Hong, Y.: An updated moving window algorithm for  
768 hourly-scale satellite precipitation downscaling: A case study in the Southeast Coast of China, *J. Hydrol.*, 581, 124378,  
769 <https://doi.org/10.1016/j.jhydrol.2019.124378>, 2020a.

770 Ma, Z., Xu, J., Ma, Y., Zhu, S., He, K., Zhang, S., Ma, W., and Xu, X.: AERA5-Asia: A Long-Term Asian Precipitation  
771 Dataset (0.1°, 1-hourly, 1951–2015, Asia) Anchoring the ERA5-Land under the Total Volume Control by APHRODITE,  
772 *B. Am. Meteorol. Soc.*, 103, E1146-E1171, <https://doi.org/10.1175/BAMS-D-20-0328.1>, 2022.

773 Ma, Z., Xu, J., Zhu, S., Yang, J., Tang, G., Yang, Y., Shi, Z., and Hong, Y.: AIMERG: a new Asian precipitation dataset  
774 (0.1°/half-hourly, 2000–2015) by calibrating the GPM-era IMERG at a daily scale using APHRODITE, *Earth Syst. Sci.  
775 Data*, 12, 1525–1544, <https://doi.org/10.5194/essd-12-1525-2020>, 2020b.

776 Mao, Y., Crow, W. T., and Nijssen, B.: A Framework for Diagnosing Factors Degrading the Streamflow Performance  
777 of a Soil Moisture Data Assimilation System, *J. Hydrometeorol.*, 20, 79-97, <https://doi.org/10.1175/JHM-D-18-0115.1>,  
778 2019.

779 Maraun, D., Wetterhall, F., Ireson, A., Chandler, R., Kendon, E., Widmann, M., Brienen, S., Rust, H., Sauter, T., and  
780 Themeßl, M.: Precipitation downscaling under climate change: Recent developments to bridge the gap between  
781 dynamical models and the end user, *Rev. Geophys.*, 48, <https://doi.org/10.1029/2009RG000314>, 2010.

782 Maselli, F., Chiesi, M., Angeli, L., Fibbi, L., Rapi, B., Romani, M., Sabatini, F., and Battista, P.: An improved NDVI-  
783 based method to predict actual evapotranspiration of irrigated grasses and crops, *Agr. Water Manage.*, 233, 106077,  
784 <https://doi.org/10.1016/j.agwat.2020.106077>, 2020.

785 Massari, C., Brocca, L., Moramarco, T., Tramblay, Y., and Didon Lescot, J.-F.: Potential of soil moisture observations  
786 in flood modelling: Estimating initial conditions and correcting rainfall, *Adv. Water Resour.*, 74, 44-53,  
787 <https://doi.org/10.1016/j.advwatres.2014.08.004>, 2014.

788 McNally, A., Shukla, S., Arsenault, K. R., Wang, S., Peters-Lidard, C. D., and Verdin, J. P.: Evaluating ESA CCI soil  
789 moisture in East Africa, *Int. J. Appl. Earth Obs. Geoinf.*, 48, 96-109, <https://doi.org/10.1016/j.jag.2016.01.001>, 2016.

790 Mei, Y., Maggioni, V., Houser, P., Xue, Y., and Rouf, T.: A nonparametric statistical technique for spatial downscaling  
791 of precipitation over High Mountain Asia, *Water Resour. Res.*, 56, e2020WR027472,  
792 <https://doi.org/10.1029/2020WR027472>, 2020.

793 Merlin, O., Walker, J. P., Chehbouni, A., and Kerr, Y.: Towards deterministic downscaling of SMOS soil moisture using  
794 MODIS derived soil evaporative efficiency, *Remote Sens. Environ.*, 112, 3935-3946,  
795 <https://doi.org/10.1016/j.rse.2008.06.012>, 2008.



796 Min, X., Ma, Z., Xu, J., He, K., Wang, Z., Huang, Q., and Li, J.: Spatially Downscaling IMERG at Daily Scale Using  
797 Machine Learning Approaches Over Zhejiang, Southeastern China, *Front. Earth Sci.*, 8,  
798 <https://doi.org/10.3389/feart.2020.00146>, 2020.

799 Mishra, V., Ellenburg, W. L., Griffin, R. E., Mecikalski, J. R., Cruise, J. F., Hain, C. R., and Anderson, M. C.: An initial  
800 assessment of a SMAP soil moisture disaggregation scheme using TIR surface evaporation data over the continental  
801 United States, *Int. J. Appl. Earth Obs. Geoinf.*, 68, 92-104, <https://doi.org/10.1016/j.jag.2018.02.005>, 2018.

802 Mu, Q., Jones, L. A., Kimball, J. S., McDonald, K. C., and Running, S. W.: Satellite assessment of land surface  
803 evapotranspiration for the pan-Arctic domain, *Water Resour. Res.*, 45, <https://doi.org/10.1029/2008WR007189>, 2009.

804 Muelchi, R., Ressler, O., Schwanbeck, J., Weingartner, R., and Martius, O.: An ensemble of daily simulated runoff data  
805 (1981–2099) under climate change conditions for 93 catchments in Switzerland (Hydro-CH2018-Runoff ensemble),  
806 *Geosci. Data J.*, <http://doi.org/10.5281/zenodo.3937485>, 2021.

807 Munsri, A., Kesarkar, A., Bhate, J., Panchal, A., Singh, K., Kutty, G., and Giri, R.: Rapidly intensified, long duration  
808 North Indian Ocean tropical cyclones: Mesoscale downscaling and validation, *Atmos. Res.*, 259, 105678,  
809 <https://doi.org/10.1016/j.atmosres.2021.105678>, 2021.

810 Nagler, P. L., Cleverly, J., Glenn, E., Lampkin, D., Huete, A., and Wan, Z.: Predicting riparian evapotranspiration from  
811 MODIS vegetation indices and meteorological data, *Remote Sens. Environ.*, 94, 17-30,  
812 <https://doi.org/10.1016/j.rse.2004.08.009>, 2005a.

813 Nagler, P. L., Scott, R. L., Westenburg, C., Cleverly, J. R., Glenn, E. P., and Huete, A. R.: Evapotranspiration on western  
814 U.S. rivers estimated using the Enhanced Vegetation Index from MODIS and data from eddy covariance and Bowen  
815 ratio flux towers, *Remote Sens. Environ.*, 97, 337-351, <https://doi.org/10.1016/j.rse.2005.05.011>, 2005b.

816 Neinavaz, E., Skidmore, A. K., and Darvishzadeh, R.: Effects of prediction accuracy of the proportion of vegetation  
817 cover on land surface emissivity and temperature using the NDVI threshold method, *Int. J. Appl. Earth Obs. Geoinf.*, 85,  
818 101984, <https://doi.org/10.1016/j.jag.2019.101984>, 2020.

819 Pan, L., Xia, H., Zhao, X., Guo, Y., and Qin, Y.: Mapping Winter Crops Using a Phenology Algorithm, Time-Series  
820 Sentinel-2 and Landsat-7/8 Images, and Google Earth Engine, *Remote Sens.*, 13, 2510,  
821 <https://doi.org/10.3390/rs13132510>, 2021.

822 Peng, J., Loew, A., Zhang, S., Wang, J., and Niesel, J.: Spatial Downscaling of Satellite Soil Moisture Data Using a  
823 Vegetation Temperature Condition Index, *IEEE Trans. Geosci. Remote Sens.*, 54, 558-566,  
824 <https://doi.org/10.1109/TGRS.2015.2462074>, 2016.

825 Peng, J., Albergel, C., Balenzano, A., Brocca, L., Cartus, O., Cosh, M. H., Crow, W. T., Dabrowska-Zielinska, K.,  
826 Dadson, S., Davidson, M. W. J., de Rosnay, P., Dorigo, W., Gruber, A., Hagemann, S., Hirschi, M., Kerr, Y. H.,  
827 Lovergine, F., Mahecha, M. D., Marzahn, P., Mattia, F., Musial, J. P., Preuschmann, S., Reichle, R. H., Satalino, G.,  
828 Silgram, M., van Bodegom, P. M., Verhoest, N. E. C., Wagner, W., Walker, J. P., Wegmüller, U., and Loew, A.: A  
829 roadmap for high-resolution satellite soil moisture applications – confronting product characteristics with user  
830 requirements, *Remote Sens. Environ.*, 252, 112162, <https://doi.org/10.1016/j.rse.2020.112162>, 2021.

831 Piles, M., Sanchez, N., Vall-Ilossera, M., Camps, A., Martinez-Fernandez, J., Martinez, J., and Gonzalez-Gambau, V.:  
832 A Downscaling Approach for SMOS Land Observations: Evaluation of High-Resolution Soil Moisture Maps Over the  
833 Iberian Peninsula, *IEEE J. Sel. Topics Appl. Earth Observ. in Remote Sens.*, 7, 3845-3857,  
834 <https://doi.org/10.1109/JSTARS.2014.2325398>, 2014.

835 Prakash, S., Mitra, A. K., Pai, D. S., and AghaKouchak, A.: From TRMM to GPM: How well can heavy rainfall be  
836 detected from space?, *Adv. Water Resour.*, 88, 1-7, <https://doi.org/10.1016/j.advwatres.2015.11.008>, 2016.

837 Quiroz, R., Yarlequé, C., Posadas, A., Mares, V., and Immerzeel, W. W.: Improving daily rainfall estimation from NDVI  
838 using a wavelet transform, *Environ. modell. softw.*, 26, 201-209, <https://doi.org/10.1016/j.envsoft.2010.07.006>, 2011.

839 Rockel, B.: The regional downscaling approach: a brief history and recent advances, *Curr. Clim. Change. Rep.*, 1, 22-  
840 29, <https://doi.org/10.1007/s40641-014-0001-3>, 2015.

841 Rozante, J. R., Gutierrez, E. R., Fernandes, A. d. A., and Vila, D. A.: Performance of precipitation products obtained  
842 from combinations of satellite and surface observations, *Int. J. Remote Sens.*, 41, 7585-7604,  
843 <https://doi.org/10.1080/01431161.2020.1763504>, 2020.

844 Sabaghy, S., Walker, J. P., Renzullo, L. J., Akbar, R., Chan, S., Chaubell, J., Das, N., Dunbar, R. S., Entekhabi, D.,  
845 Gevaert, A., Jackson, T. J., Loew, A., Merlin, O., Moghaddam, M., Peng, J., Peng, J., Piepmeier, J., Rüdiger, C., Stefan,  
846 V., Wu, X., Ye, N., and Yueh, S.: Comprehensive analysis of alternative downscaled soil moisture products, *Remote*  
847 *Sens. Environ.*, 239, 111586, <https://doi.org/10.1016/j.rse.2019.111586>, 2020.

848 Salzmann, M.: Global warming without global mean precipitation increase?, *Sci. Adv.*, 2, e1501572, [https://doi.org/](https://doi.org/10.1126/sciadv.1501572)  
849 [10.1126/sciadv.1501572](https://doi.org/10.1126/sciadv.1501572), 2016.

850 Senanayake, I. P., Yeo, I. Y., Willgoose, G. R., and Hancock, G. R.: Disaggregating satellite soil moisture products  
851 based on soil thermal inertia: A comparison of a downscaling model built at two spatial scales, *J. Hydrol.*, 594, 125894,  
852 <https://doi.org/10.1016/j.jhydrol.2020.125894>, 2021.

853 Seneviratne, S. I., Corti, T., Davin, E. L., Hirschi, M., Jaeger, E. B., Lehner, I., Orlowsky, B., and Teuling, A. J.:  
854 Investigating soil moisture–climate interactions in a changing climate: A review, *Earth Sci. Rev.*, 99, 125-161,  
855 <http://dx.doi.org/10.1016/j.earscirev.2010.02.004>, 2010.

856 Sheffield, J., Ferguson, C. R., Troy, T. J., Wood, E. F., and McCabe, M. F.: Closing the terrestrial water budget from  
857 satellite remote sensing, *Geophys. Res. Lett.*, 36, <https://doi.org/10.1029/2009GL037338>, 2009.

858 Shen, Y., Xiong, A., Hong, Y., Yu, J., Pan, Y., Chen, Z., and Saharia, M.: Uncertainty analysis of five satellite-based  
859 precipitation products and evaluation of three optimally merged multi-algorithm products over the Tibetan Plateau, *Int.*  
860 *J. Climatol.*, 35, 6843-6858, <https://doi.org/10.1080/01431161.2014.960612>, 2014.

861 Song, S., Brocca, L., Wang, W., and Cui, W.: Testing the potential of soil moisture observations to estimate rainfall in a  
862 soil tank experiment, *J. Hydrol.*, 581, 124368, <https://doi.org/10.1016/j.jhydrol.2019.124368>, 2020.

863 Sorooshian, S., Hsu, K.-L., Gao, X., Gupta, H. V., Imam, B., and Braithwaite, D.: Evaluation of PERSIANN system  
864 satellite-based estimates of tropical rainfall, *B. Am. Meteorol. Soc.*, 81, 2035-2046, <https://doi.org/10.1175/1520-0477>,  
865 2000.

866 Spötl, C., Koltai, G., Jarosch, A., and Cheng, H.: Increased autumn and winter precipitation during the Last Glacial  
867 Maximum in the European Alps, *Nat. Commun.*, 12, 1-9, <https://doi.org/10.1038/s41467-021-22090-7>, 2021.

868 Tagesson, T., Horion, S., Nieto, H., Zaldo Fornies, V., Mendiguren González, G., Bulgin, C. E., Ghent, D., and Fensholt,  
869 R.: Disaggregation of SMOS soil moisture over West Africa using the Temperature and Vegetation Dryness Index based  
870 on SEVIRI land surface parameters, *Remote Sens. Environ.*, 206, 424-441, <https://doi.org/10.1016/j.rse.2017.12.036>,  
871 2018.

872 Tang, G., Behrangi, A., Long, D., Li, C., and Hong, Y.: Accounting for spatiotemporal errors of gauges: A critical step  
873 to evaluate gridded precipitation products, *J. Hydrol.*, 559, 294-306, <https://doi.org/10.1016/j.jhydrol.2018.02.057>, 2018.

874 Tang, J., Niu, X., Wang, S., Gao, H., Wang, X., and Wu, J.: Statistical downscaling and dynamical downscaling of  
875 regional climate in China: Present climate evaluations and future climate projections, *J. Geophys. Res. - Atmos.*, 121,  
876 2110-2129, <https://doi.org/10.1002/2015JD023977>, 2016.

877 Wackernagel, H.: Ordinary kriging, in: *Multivariate geostatistics*, Springer, 79-88, 2003.

878 Wehbe, Y., Temimi, M., and Adler, R. F.: Enhancing precipitation estimates through the fusion of weather radar, satellite  
879 retrievals, and surface parameters, *Remote Sens.*, 12, 1342, <https://doi.org/10.3390/rs12081342>, 2020.

880 Wehbe, Y., Ghebreyesus, D., Temimi, M., Milewski, A., and Al Mandous, A.: Assessment of the consistency among  
881 global precipitation products over the United Arab Emirates, *Hydrol. Reg. Stud.*, 12, 122-135,  
882 <https://doi.org/10.1016/j.ejrh.2017.05.002>, 2017.

883 Wei, K., Ouyang, C., Duan, H., Li, Y., Chen, M., Ma, J., An, H., and Zhou, S.: Reflections on the Catastrophic 2020  
884 Yangtze River Basin Flooding in Southern China, *The Innovation*, 1, 100038,  
885 <https://doi.org/10.1016/j.xinn.2020.100038>, 2020.

886 Wen, F., Zhao, W., Wang, Q., and Sánchez, N.: A Value-Consistent Method for Downscaling SMAP Passive Soil  
887 Moisture With MODIS Products Using Self-Adaptive Window, *IEEE Trans. Geosci. Remote Sens.*, 58, 913-924,  
888 <https://doi.org/10.1109/TGRS.2019.2941696>, 2020.

889 Xia, T., Wang, Z.-J., and Zheng, H.: Topography and Data Mining Based Methods for Improving Satellite Precipitation  
890 in Mountainous Areas of China, *Atmosphere*, 6, 983-1005, <https://doi.org/10.3390/atmos6080983>, 2015.

891 Xu, J., Ma, Z., Yan, S., and Peng, J.: Do ERA5 and ERA5-land precipitation estimates outperform satellite-based  
892 precipitation products? A comprehensive comparison between state-of-the-art model-based and satellite-based  
893 precipitation products over mainland China, *J. Hydrol.*, 605, 127353, <https://doi.org/10.1016/j.jhydrol.2021.127353>,  
894 2022.

895 Xu, S., Wu, C., Wang, L., Gonsamo, A., Shen, Y., and Niu, Z.: A new satellite-based monthly precipitation downscaling  
896 algorithm with non-stationary relationship between precipitation and land surface characteristics, *Remote Sens. Environ.*,  
897 162, 119-140, <https://doi.org/10.1016/j.rse.2015.02.024>, 2015.

898 Yan, X., Chen, H., Tian, B., Sheng, S., and Kim, J. S.: A Downscaling–Merging Scheme for Improving Daily Spatial  
899 Precipitation Estimates Based on Random Forest and Cokriging, *Remote Sens.*, 13, 2040,  
900 <https://doi.org/10.3390/rs13112040>, 2021.

901 Yang, X. and Huang, P.: Restored relationship between ENSO and Indian summer monsoon rainfall around 1999/2000,  
902 *The Innovation*, 2, 100102, <https://doi.org/10.1016/j.xinn.2021.100102>, 2021.

903 Zambrano-Bigiarini, M., Nauditt, A., Birkel, C., Verbist, K., and Ribbe, L.: Temporal and spatial evaluation of satellite-  
904 based rainfall estimates across the complex topographical and climatic gradients of Chile, *Hydrol. Earth Syst. Sci.*, 21,  
905 1295–1320, <https://doi.org/10.5194/hess-21-1295-2017>, 2017.

906 Zeng, Z., Chen, H., Shi, Q., and Li, J.: Spatial Downscaling of IMERG Considering Vegetation Index Based on Adaptive  
907 Lag Phase, *IEEE Trans. Geosci. Remote Sens.*, 1-15, <https://doi.org/10.1109/TGRS.2021.3070417>, 2021.

908 Zhan, C., Han, J., Hu, S., Liu, L., and Dong, Y.: Spatial Downscaling of GPM Annual and Monthly Precipitation Using  
909 Regression-Based Algorithms in a Mountainous Area, *Adv. Meteorol.*, 2018, 1506017,  
910 <https://doi.org/10.1155/2018/1506017>, 2018.

911 Zhang, H., Ma, J., Chen, C., and Tian, X.: NDVI-Net: A fusion network for generating high-resolution normalized  
912 difference vegetation index in remote sensing, *ISPRS J. Photogramm. Remote Sens.*, 168, 182-196,  
913 <https://doi.org/10.1016/j.isprsjprs.2020.08.010>, 2020a.

914 Zhang, L., Ren, D., Nan, Z., Wang, W., Zhao, Y., Zhao, Y., Ma, Q., and Wu, X.: Interpolated or satellite-based  
915 precipitation? Implications for hydrological modeling in a meso-scale mountainous watershed on the Qinghai-Tibet  
916 Plateau, *J. Hydrol.*, 583, 124629, <https://doi.org/10.1016/j.jhydrol.2020.124629>, 2020b.

917 Zhao, W., Sánchez, N., Lu, H., and Li, A.: A spatial downscaling approach for the SMAP passive surface soil moisture  
918 product using random forest regression, *J. Hydrol.*, 563, 1009-1024, <https://doi.org/10.1016/j.jhydrol.2018.06.081>, 2018.

919 Zhao, W., Wen, F., Wang, Q., Sanchez, N., and Piles, M.: Seamless downscaling of the ESA CCI soil moisture data at  
920 the daily scale with MODIS land products, *J. Hydrol.*, 603, 126930, <https://doi.org/10.1016/j.jhydrol.2021.126930>, 2021.